Numerical simulation of debris throw after breaking up of a concrete structure by blast load

Xiong Can

School of Civil and Environmental Engineering

A Thesis submitted to the Nanyang Technological University
in the fulfillment of the requirement for the degree of
Master of Engineering

2008

Acknowledgements

I would like to express my most sincere gratitude to my supervisor, Prof. Fan Sau Cheong, for his constant guidance, encouragement, and support throughout my graduate study at NTU. His open-mindedness and kindness have been inspiring to me.

I am grateful to Dr. Yu Qingjun for his instructions and guidance on numerical studies and Dr. Li Yong for his patient and helpful explanation on the program codes.

My thanks also go to Dr. Yang Yaowen and Lim Heng Soon from Defense Science and Technology Agency for their insightful comments to improve the research.

This study was conducted under Dual Degree Master Program, the cooperation between Nanyang Technological University and Shanghai Jiao Tong University. I would also like to thank my co-supervisor Prof. Zhao Jincheng from SJTU for his help to joining the program.

My deepest appreciation is reserved for my family. I am extremely grateful to my parents, Xiong Bailiang and Xu Meiru. Their enduring love and trust are the foundations of my every achievement. I dedicate this thesis to them. I want to thank my boyfriend, Liu Xiuyuan, for his love and moral support from my home country of China.

Table of Contents

Summary

Earth-covered structures are widely applied in military defense engineering, mainly to protect against the external impact of missiles and blast, while Earth-Covered Magazines (ECM) are also used to store explosive materials and munitions, and therefore the study of internal detonation is required. The debris throw distance after an accidental explosion in ammunition magazines is often one of the most important hazard parameters.

The high preparation cost and safety concerned for carrying out a high-density load test on a structure often place a curb upon many field tests. A feasible alternative is to harness the power of the computing technology to conduct numerical simulations, together with verification by a limited number of field tests.

The numerical simulation of debris hazards study includes two parts: magazine break-up under internal detonation and the subsequent calculation of debris throw. Most effort is made to solve the second part in this thesis.

For the debris throw pattern part, a Visual C++ (6.0) program is employed, while the solid structure response simulation is done by the software LS-DYNA. The whole simulation process, from the detonation of the explosives to the landing of the debris is done by the two programs continuously by data transfer. All the input data of the C++ program is derived from calculation results of the simulation done by LS-DYNA.

Numerical simulations are carried out for various cases. Simulations for debris throw are performed after the blast overpressure dropped to zero. The debris scattering patterns are investigated and presented in statistical terms.

Statement of novelty

One of the novelties of the research in this thesis is the combination of methods to simulate the blasting debris. Program LS-DYNA and a code in Visual C++ (6.0) are involved. It is more direct way to analysis the debris hazards than other methods which are more or less rely on statistic and probability.

List of tables

List of figures

List of symbols

V	velocity of debris
V_x	velocity in horizontal direction of debris
V_y	velocity in vertical direction of debris
a	acceleration of debris
φ	angular acceleration of debris
(x, y)	Cartesian coordinates of the debris
θ	slope of the debris trajectory to the horizontal
g	acceleration due to gravity
V_0	initial or the ejective velocity of debris
θ_0	initial or the ejective angle of debris
V_k	landing velocity when debris hits the ground
θ_k	landing angle when debris hits the ground
V_a	velocity a when debris gets to the vertex of the trajectory
x_a	horizontal displacement when debris gets to the vertex
H	vertex height of debris trajectory
L	debris horizontal displacement before it hits the ground.

F_d	drag force experienced by debris
C_d	drag coefficient of debris
Re	Reynolds number

List of publications

Journal paper

Xiong, C., Zhao, J.C., et al, (2008) "Numerical simulation and analysis of the debris throw and scattering pattern after blast of a concrete structure", Blasting (under review)

1. Introduction

1.1 Research objectives

Earth-covered structures are widely applied in military defense engineering, mainly to protect against the external impact of missiles and blast, while Earth-Covered Magazines (ECM) are also used to store explosive materials and munitions, and so the study of internal detonation is required.The debris throw distance after an accidental explosion in ammunition magazines is often one of the most important hazard parameter.

Testing of magazines generally began from 1945, with the aim to provide safe and land saving designs. The internal detonation test of magazines is mainly to get the overall structural response, airblast measurements, and hazardous fragment distribution in terms of densities, weights, and their locations relative to magazine orientation. The design requirements of minimum safe separation distances between earth-covered magazines and the distances between inhabited buildings and the earth-covered magazines concerned are determined based on the hazards of fragment and peak overpressure.

The high preparation cost and safety concerned for carrying out a high-density load test on a structure often place a curb upon many field tests. A feasible alternative is to harness the power of the computing technology to conduct numerical simulations, together with verification by a limited number of field tests.

The numerical simulation of debris hazards study includes two parts: magazine break-up under internal detonation and the calculation of debris throw. Most effort is made to solve the second part in this thesis.

1.2 Research methodology

For the break-up of reinforced concrete (RC) structure subjected to internal high-density blast load, a novel numerical simulation scheme, which combines the nodal splitting method and element erosion method, is employed in LS-DYNA program.

The solid in the simulation model includes concrete and reinforced steel bar, which are modelled using the Lagrangian method by the finite element method (FEM). The fluid part including air and TNT is modelled using the Eulerian method by the finite difference method (FDM). They are coupled using the constrained Lagrange in solid, which provides the mechanism for coupling interaction between a slave Lagrange geometric entity and a master Eulerian geometric entity, through spring penalty method to effectively simulate the interaction between the solid and fluid parts.

For the debris throw pattern part, a Visual C++ (6.0) program is employed, while the solid structure response simulation is done by the software LS-DYNA. The whole simulation process, from the detonation of the explosives to the landing of the debris is done by the two programs continuously by the data transfer. All the input data of C++ program is derived from calculation results of the simulation done by LS-DYNA.

At the beginning of the C++ program, the definition of the fragment / debris is done. Then the program starts to simulate the debris throw motion. At last the debris scattering pattern is analyzed.

The parameters and coefficients used in the simulation are based on the previous research and scientific judgment firstly. As the first round simulation done, the results are compared with the test results to modify the parameters and coefficients.

1.3 Research scope

This thesis will look into the structure break-up pattern and study debris distribution of reinforced concrete magazines with/without earth covered under internal detonation using the above mentioned new method, combining the program LS-DYNA and a code in C++ (6.0), with different charge stack format (centered and distributed) and loading density (2.5kg/m^3 and 30kg/m^3). The emphasis is given to the debris scattering pattern.

As the methodology of modelling solid structure response is relatively mature; therefore, emphasis of the research is to investigate the debris scattering pattern. Subjects like the equations of motions of a single debris, the drag force and drag coefficient of debris, debris projectile velocity and angle, etc. are concerned.

The structure break-up and deformation pattern are discussed. Results of debris throw after breaking up are presented by details and analyzed.

1.4 Organisation of the thesis

Chapter 2 is on literature review of various resources of the debris, debris hazard prediction tools and models and the field test against those tools.

In Chapter 3, the review of related object motion and equations is presented first. Then the adoption of the equations of motion is given.

In Chapter 4, the review of the air drag of the motion is followed by the determination the drag force experienced the debris. Specific attention is assigned to the drag coefficient.

Chapter 5 discusses the blast debris simulation algorithm. A novel combined algorithm with three criteria is introduced first. The information managing and debris defining algorithms are then presented. Last, the validity of the algorithms is looked into.

In chapter 6, the overall parameters of the simulated models are presented first. The finite element model is described, including the mesh and material information. The results of the break-up and deformation are illustrated mainly by the picture captured during the process. Last, the results of the debris throw are given and discussed.

Chapter 7 gives the main conclusions of the thesis and the recommendations to continue the research on debris hazards analysis.

2. Literature review

2.1 Overview

Research on debris trajectory is not completely new. There are various resources of the debris, which are containing the debris of the space shuttles and aircrafts, wind-borne debris, debris after controlled demolition blast, et al.

The hazards of those debris are one of the most concerned objects in the research. Therefore the characteristics of the debris, like the initial velocity and projectile angle, the shape of the debris, mass and volume of the debris, are studied for the prediction of the hazards. Since the basic information about the debris has been obtained more or less, together with other knowledge, the hazards prediction model and tool have been generated and upgraded by different research groups.

The field tests and other kinds of explosion tests results provide the data for the parameters and the coefficients employed in the prediction models. The successive test results enable the modification and completion of models.

2.2 Debris from broken space vehicle and aircraft

As the rocket components are recycled to maximize the economic benefits, the trajectory analysis of the separating descent part is essential. The trajectory coefficient G/C_DA (weight to drag ratio) (Lin 1999) is very important in the trajectory analysis, which give a direct prediction of the recycling site.

During ascent process, the space shuttle may hit by some small part separated from it. If the impact velocity is high enough, the collision causes damage to the shuttle or even huge loss.

Video analysis of an ascent of space shuttle in January 2003 showed that an object shed from the bipod-ramp region impacted the left wing of the orbiter (Columbia Accident Investigation Board 2003). The analysis both during and after the mission provided an accurate prediction of the velocity of a large piece of the left foam bipod ramp would have as it impacted the wing leading edge. The prediction was corroborated by both the video analysis and fully coupled CFD/6-DOF simulation. The concerns with predicting the aerodynamic characteristics of a variety of potential debris sources (insulating foam, ice, ...) for the Space Shuttle Launch Vehicle (SSLV) using Computational Fluid Dynamics (CFD) methods were presented in Murman's AIAA paper (Murman 2005).

In his paper, the CFD method was introduced as an effective tool to simulate debris trajectories, which were highly non-linear, involving uncontrolled three-axis rotations. While the traditional aerodynamic modeling techniques developed for controlled maneuvers of aerodynamically-trim aircraft were not sufficient.

The Federal Aviation Administration of United States (FAA) had presented an airframe disintegration debris scatter distance formula in its publication (FAA a; FAA b). The formula stated that the scatter distance was equal to the aircraft's speed times the square root of two times the aircraft's altitude divided by the acceleration of gravity. The FAA Formula limited its variable inputs to those of aircraft speed and altitude, while neglecting the projectile's weight, frontal area, drag characteristics, and angle of separation. Further, no allowance was made for wind effect or density altitude. These variables would dramatically influence the projectile's down range capabilities.

As the FAA Formula was inadequate for use in an objective, analytical evaluation of airshow maneuvers directed at the spectator area and the establishment of safe spectator separation distances for these maneuvers, the information and data needed

in the analytical study of in-flight airframe disintegration debris scatter patterns were presented by Oldham in his report (Oldham 1990).

The computer program employed by him took the following information as input data: initial altitude of disintegration and density altitude, altitude of impact at ground level, wind velocity and direction, horizontal true airspeed at disintegration, rate of climb or sink at disintegration, weight, drag coefficient and frontal area of projectile. The program then gave the output data: horizontal distance form disintegration at impact, horizontal, vertical and total velocities, terminal velocity, time to fall, flight-path angle at impact, ground speed of projectile at impact and x and z components of that velocity.

2.3 Debris from tornado

Windborne debris is possibly the major cause of building damage and destruction in strong wind events such as hurricanes and tornadoes (Lin 2005). It has been long recognized that fast-flying debris can penetrate building envelopes. Consequently, failed roofing structures, damaged wall cladding panels, and broken glass become debris sources, threatening downwind areas.

Early in the 1970's, McDonald (McDonald 1976) claimed that the biggest problem in tornado-resistant design of nuclear power plants and structures is protection from missiles. Minor (Minor 1994) reported several serious window damage caused by windborne debris in American. Lee and Wills (Lee and Wills 2002) presented another significant glazing damage happened in Hong Kong. In order to prevent such damages to the buildings, the building envelopes should be built resist debris impact. Several impact tests were carried out by McDonald (McDonald 1990; McDonald 1999) and Minor (Minor 1994).

The research on the debris trajectories is dated back to 1970's. The debris trajectory model has been developed from a simple one to the most complicated 6D model. Simiu and Cordes (Simiu and Cordes 1976) developed a particle model considered

only the drag force on the debris. Lee's (Lee 1974) model of tornado-generated missiles considered both drag and lift forces, resulted in two significant parameters for missile initiation, C_DA/W and C_LA/W (C_D and C_L are the drag and lift coefficient of the debris, A is the reference debris area, W is the weight of the debris); however, C_D and C_L were considered to be constants during the flight. A 3D random orientation model which considered random drag, lift and side force coefficients varying with the orientation of the missile with respect to the relative wind vector was developed by Twisdale et al (Twisdale 1979). A full 6D trajectory model considering pitching, rolling and yawing moments, as well as drag, lift, and side forces was generated by Redmann (Redmann, Radbill et al. 1976) at last.

With an average value for drag coefficient over the flight, Holmes (Holmes and English 2004) calculated the trajectory of 'compact' debris, such as cubes and spheres. The numerical solutions of 'compact', plate and rod debris trajectories were discussed by Backer (Baker 2004).

The wind-tunnel experiments results on drag, lift and moment force coefficients were compared with the numerical simulation by Tachikawa (Tachikawa 1983), who was the first person to combine the experimental and simulation methods together. Then Backer (Baker 2004) compared his numerical debris trajectory with Tachikawa's obtained from experiments. Holmes (Holmes, Letchford et al. 2006) solved the trajectory of square plates and this numerical result was compared to their own wind-tunnel experimental results.

There had been two ways to analyze the risk brought in by debris. They were deterministic and probabilistic methods. Because of the inherent uncertainties of the windborne debris problems, the probabilistic methods were employed to solve them. The probabilistic approach often involves Monte Carlo simulation. The Monte Carlo simulation performed in the risk-based design included three deterministic models: wind field description, debris generation, and debris trajectory(Twisdale, Vickery et al. 1996).

2.4 Debris from demolition blasting

In controlled demolition blasting operation, the flying range of the rock and stones projected by the explosion effect was usually calculated without air drag (Qin 1991). In other words, the estimated safe clearance was the maximum flying range when the air drag was set to be zero. In the application of the controlled demolition blasting in urban areas, some equipment is fixed to protect against the flying debris. Therefore, a series of modification coefficient was introduced into the range estimation formula (Fan, Shen et al. 2002). If the blasting was conducted in the mountain areas, the safe clearance error caused by the elevation must be considered (Kang 1999).

More details about application of directional demolition blasting in the mining industry were concerned. The drag force experienced by the rock, the trajectory and the flying range of the rock were discussed (Черниговский and Shi 1982). The ballistic table for calculating the rock trajectory was derived as well. However, the important coefficient in the trajectory calculation, such as the drag coefficient, was employed as the empirical value without experimental verification. Further, the rock projectile velocity was limited under 100 m/s, confirming to the realistic situation.

2.5 Prediction tool and model for blasting debris

An accidental detonation in an ammunition magazine will lead to break-up of the construction and the throw of debris. The chain of events consists of (i) the internal explosive loading of the donor structure, (ii) donor break-up and debris launch, (iii) debris throw and (iv) impact on the acceptor (structure or person) by the generated blast and debris. The quantitative assessment models for this chain of events are the backbone of the risk analysis tools.

Generally, several models have been developed by different research groups for different specific objectives. For different objectives, the chain of events is modeled

at different level of details. Some of the model information is presented below, with the details on the debris throw.

2.5.1 Quantity-Distance (QD) model

In order to provide an approved method for determining sitting distances for explosive loading conditions and different building construction types, an analytical model was presented to predict hazardous building debris distances for accidental explosions within explosives material operations buildings, under the funding by U.S. Department of Energy (DOE) Safety Office and the U.S. Department of Defense Explosives Safety Board (DDESB). The model, as a sitting tool, is able to predict debris distances using similar loading conditions in buildings constructed of various materials, such as reinforce concrete (RC), masonry, etc., and the combination of these materials. Verification and refinement of the model are based on data from an extensive test program (DDESB 1991).

The model is divided into several components according to the analysis procedure. They are loading prediction on internal surfaces, prediction of structure breakup and determination of debris characteristics, such as debris mass, velocity, angle and drag, debris dispersion and debris tumble, ricochet and roll after impact. These calculation codes are modified based on the statistic analysis of the supporting tests and observations from the tests.

Debris dispersion is predicted by the computer program MUDEMMIMP using input probability distribution to describe building breakup, accounting for drag effects as well. The debris mass distribution is assigned to be exponential. The debris initial velocity and angle distributions are assigned to be normal. The drag coefficient distribution is assigned to be uniform or constant, depending on the material. The drag area factor distribution is assigned to be constant. The input for the drag coefficient distribution, such as reinforced concrete, is a uniform distribution varying between 1.0 and 2.0.

2.5.2 SAFER model

The SAFER model is developed for the DDESB and military services (Weerheijm, Norman et al. 2008). It is a risk-based approach for explosive safety analysis and a probabilistic model. SAFER provides methodologies for calculating the risk associated with explosives operations and storage. The three elements of the methodology are the probability of event, probability of fatality given an event, and exposed personnel. The predictions of the break-up of the structure and debris throw are the essential parts of the methodology to quantity the risks. However, the debris information is not specifically the goal of the program.

There are three categories debris evaluated separately in the program. They are primary debris from the explosive item, secondary debris from the Potential Explosion Site (PES), and ejacta from the crater. The trajectories of the secondary debris are not calculated individually, but rather are broken into categories: lobbed, depressed trajectory, and low-angle fragments moving nearly parallel to the ground with speeds exceeding terminal velocity. The distribution of pieces is assumed to have a bivariate normal shape.

2.5.3 KG-E Tool and software

Another engineering predictive tool for debris throw from reinforced concrete structure after the detonation of a bare charge is called KG-E Tool, developed by the Klotz Group (international group of experts on explosive safety)(Dörr, van der Voort et al. 2008). The relations for distribution of debris mass, launch velocity and launch angle, as a function of the loading density and wall thickness are based on the state of art knowledge and debris pick-up data from trials.

The trajectories of projectiles in this model are accounted for air drag and gravity. The lift force is neglected for the practical services and the density of air is treated as a constant. The debris drag coefficient is in a function of its velocity, related to Mach number (van der Voort 2008).

Based on the observation of the practical calculation results some simplifications are introduced into the trajectory calculation, such as horizontal drag approximation, no drag limit and close-in limit (van der Voort 2008). For the debris with the launch angle close the normal direction of the wall, the horizontal component of the drag force is much larger than the vertical one. According to this phenomenon, the equations of motion are simplified by 'decoupling'. The no drag limit is more suitable for the debris with small initial velocity. Debris with the trajectories being well approximated by straight line is taking close-in limit.

In KG- E Tool, the throw of debris from the source with arbitrary geometry and for arbitrary initial conditions, which are defined by the distribution of mass, launch velocity and launch angle, is described by the deterministic model using source function theorem, an underlying mathematical relation between the debris density and the initial distributions, while the Monte Carl Technique is used by other models (van der Voort, van Doormaal et al. 2008).

The backward calculation kernel, which is used to derive information on the initial launch velocity and angular distribution, enabling the future updates of the software based on the new tests data, is embedded into the Tool (Dörr, van der Voort et al. 2008).

2.5.4 UK model

A modularized program, UK model has been developed to predict the break-up of ammunition store house and final resting point of debris to determining Inhabited Building Distances (IBD) and generate the input data for lethality models (Weerheijm, Norman et al. 2008). It is the most deterministic model and is based on simplified 'first principle approach'. It does not use only experimental data from tests, but also depends on detailed modeling and material input at elementary material level.

In the model, the whole break scenario down into three parts: the dynamic loading profile is generated by SHOCK and FRANG, or AUTODYN for more complicated loadings, RCWall is employed to calculate the structure response and debris throw,

bounce, ricochet and roll are simulated by DEBDIS. Further, the fatality model can be added in to give the fatality probability.

2.5.5 Debris simulation by LS-DYNA

A methodology for the simulation of masonry wall failure and debris scatter under the high explosive loading within LS-DYNA was developed by McCallum et al (McCallum, Locking et al. 2008). The masonry wall failure, brick motion and drag are modeled in the single software, which is advantage of this methodology.

In that study, masonry walls made up of bricks were modeled as individual parts with tiebreak contact, which was used to define the strength of the mortar between adjacent bricks and was based on normal and shear strength failure parameters, and the single surface contact, which is used to model the interaction of bricks separated from the wall. The detonation of the explosive could be modeled by the load blast function.

The air-drag is accounted in the methodology using a user-defined load force in LS-DYNA through a FORTRAN subroutine. Then the results of the subroutine were compared with the numerical solution and a good agreement was obtained.

The images showing the collapse of the building and debris scatter were parts of the output.

2.5.6 Debris from vehicles transporting explosives

A model to evaluate the debris throw hazards from vehicles transporting explosives, both the trucks and railway cars with or without a top has been developed to serve the purpose of transportation of ammunition and explosives (TAE) risk analysis (Nussbaumer and Kummer 2008). The model is applicable for calculating the lethality distribution.

The main effort of this model is that it provides the method to transform the blasting debris densities into lethalities. Then the debris densities in the mid-to-far distance

(100 m away from detonation vehicles) and close-range distance (within 100 m),with different cover types are transformed into probit-lethality.

2.6 Field tests against prediction tool

Research of debris, including the characteristics of debris, debris throw model and debris hazards assessment are relying on the supporting tests data. The tests data is used for both the development of the debris throw models as the first-round input and the improvement after the comparing the simulation results with test results. Thus, the field test has been carried out along with the simulation efforts and has been kept on ever since.

2.6.1 SCIPAN test

The SCIPAN series test is planned to be made up of 6 tests (Swisdak, Conway et al. 2008). The full-scale donor tests are involved. Three of them have been done already. The test is aimed at addressing two issues. One is the secondary or donor (Potential Explosion Site, PES) debris generation and density versus distance and azimuth. The other is the target building (Exposed Site, ES) response to blast loading.

The loading density range of these tests is starting at 3.92 kg/m^3 up to 106.79 kg/m^3. The PES falls into two types. One is 14.6×14.6×4.9 m^3 and the other is 9.1×9.1×3.0 m^3. The ES material type is various. RC wall/Wood roof, steel frame with infill panels, metal trailer and other materials are included.

2.6.2 SPIDER test

The SPIDER is short for the Science Panel Impact Data Evaluation and Review project. The debris impact effect on exposed objectives is concerned in these tests. The series test is made up of 4 tests, one of them is finished (Swisdak, Conway et al. 2008). There are two main problems to be solved out by the test. One is relationship between material type, debris mass and velocity and perforation of and damage to

specific kind of roof and wall. Another one is assessment of the resultant hazard posed by debris perforation and damage.

The tested impactor items are generally the steel/concrete ball and steel/concrete rod. Roof and wall with different material types, such as RC, corrugated metal panel, etc., are considered as the impact targets. Only perpendicular impact angle and mid-panel impact location is tested. Both the terminal and higher-than-terminal velocities are tested in different tests.

2.6.3 ISO test

The ISO container test give the supporting data for information of debris throw from the vehicles transporting explosives more directly. The whole ISO program is made up 4 tests and two of them have been conducted already (Swisdak, Conway et al. 2008). The tests is planned to find out the debris characteristics of the ISO container, as well as the effects of container arrangements on debris production and prevention of propagation.

2.6.4 Kasun test

Kasun test is the kind of break-up test with small ammunition houses. Kasun test Ⅰ and Ⅱ have been done already. The test is set up to get experimental data related to the hazards to surroundings after an accidental explosion in an above ground ammunition magazine, including the understanding of the importance of debris bounce, roll and slide (Berglund, Carlberg et al. 2006).

In Kasun Ⅰ, experiments are performed with a maximum loading density 6.25 kg/m^3 and in all experiments the charges were put in the centre of the volumes. While in Kasun Ⅱ, the loading densities varied between 2.5 and 30 kg/m^3 and the charges more realistically located (close to the floor).

Debris throw was recorded with high speed digital video cameras during the tests and post test pick up was made to determine debris mass size distribution and location. The blast pressure around the test objects was also recorded.

2.7 Summary

In this chapter, various researches on debris have been reviewed. First debris from different resources and the debris characteristic of each category have been taken into the scope. Then the systematic debris hazards prediction models and tools are discussed and compared. The explosion tests which are the most direct data resources are presented last.

3. Equations of motion for debris

3.1 Overview

In this chapter, effort has been made to find out the suitable equations to be adopted in the C++ program for calculating the debris motion. The object (debris) motion is discussed. The equations of motion in various expressions are reviewed.

The review includes three main parts. First, vertical ball motion and projectile motion with air drag are looked back first. Then the solutions of the equations and the optimal problems are followed. Last is the related research in exterior ballistics.

3.2 Review

3.2.1 Vertical Ball Motion

Effects of air resistance on the rising and falling balls were concerned first of all as the simplification case of the projectile motion. After several experiment tests, Lindemuth (Lindemuth 1971) found that for a very light ball the surface of the ball was an important factor, but the roughness was not important factor for heavier balls. Thimmerman (Timmerman and van der Weele 1999) reviewed the problem of a vertical thrown ball, with a drag force which was either linear or quadratic in the speed. The buoyant force was also included in the treatment of the problem.

3.2.2 Projectile Motion with air drag

MacDonald (MacDonald and Hanzely 1991) compared the golf trajectories calculated using lift and drag forces based on the Erlichson model, which used drag

and lift forces that were linearly proportional to the velocity and the BH experimentally determined C_D (drag), C_L (lift) coefficients, which were quadratic proportional to the velocity. Quantitative and qualitative differences between the model predicting and experiment measure was explored, which illustrated the scientific method at work.

3.2.3 Solutions of the equations

Hayen, in his two successive papers (Hayen 2003a; Hayen 2003b), presented the exact and approximate solution of projectile motion equations. The drag force that acts upon the particle within the medium was proportional to the particle speed squared.

A new technique was introduced which provides an exact time-implicit solution to these equations in the form of a parametric description of the particle motion. This description was utilized to obtain exact conditions from which the maximum projectile range and the optimal projection angle could be determined to any desired degree of precision. This description also revealed general properties of the projectile trajectory, some of which motivated the development of an approximate solution.

A cubic polynomial form of $y = -ax^3 - bx^2 + cx$, where it had been assumed that a, b and c were positive constants were assumed to get the approximate solution, which was then utilized to obtain estimates for the maximum projectile range, optimal projection angle, and other quantities of interest related to the particle motion.

Warburton and Wang (Warburton and Wang 2004) focused on the process to get solution of the general asymptotic projectile motion equations by using the Lambert W function, without the detailed discussion on the form of the drag force.

Morales (Morales 2005) expressed the analytical solution of motion equation, with linear drag force concerned, in terms of the Lambert W function, and from those solution, a number of mathematical and numerical results obtained previously with the implicit relation for the range were obtained more easily. However, the linear

model was only an approximation for spherical objects. For radii and speeds of practical interest, more accurate models, a drag force quadratic in the velocity should be included. The solutions of the equations of motion to first order in $\delta = (n - 1)/2$ for the projectile with drag forces proportional to the nth power of the projectile's speed could be used for more general conditions.

Tan and Frick (Tan, Frick et al. 1987) followed the older approach and have obtained good results. The analytical solutions for the velocity, curvature, and arc length are obtained as functions of the slope angle and entire problem was reduced to simple integration over the slope angle.

Based on their progress, Chudinov (Chudinov 2001) developed a local analytical solution of the problem of the motion of a point mass in a medium with a square law of drag was constructed, and simple analytical formulae were obtained for the main parameters of the trajectory of the point mass. This solution differed from the other solutions in the simplicity of the formulae, ease of use, high accuracy and the absence of constraints imposed on the value of the drag.

3.2.4 Optimal Problems

Both the optimal angle of release for given projectile and initial speed, and the optimal radius for given density (i.e., among a bed of pebbles) were determined by using the drag force $F_D = C_D \rho_a \pi R^2 v^2 (-v'/v) /2$ (Zufiria and Sanmartin 1982). An increase on the height of release was found to always decrease the angle and increase the radius. A quadratic air drag was taken into account.

Another optimal problem was discussed by Price and Romano (Price and Romano 1998). They pointed out that the optimal angle of launch was greater than 45° when n, the exponent of the velocity dependence, was larger than some critical value n_{crit}, which was around 3.5, while presented in some text-books, that for any force directed opposite to the velocity of the projectile , the optimal angle could not be greater than 45°. Due to their observation, in the case of large n, the drag was

ferociously strong at the beginning of the launch, immediately slowed down the projectile to a speed at which the drag was a small force compared to the weight of the projectile. Large n drag, therefore, was confined to a very small portion of the beginning of the trajectory.

Chudinov (Chudinov 2004) used his analytical solution to solve two problems of optimization aimed at maximizing the flight range of a point mass and minimizing the initial speed of the point mass for getting to the given point on plane by presenting a baseball as an example.

Vial (Vial 2007) simplified the problem of the horizontal distance travelled by the point mass experiencing the quadratic drag force by introducing a normalized distance. The optimal angle as a function of the initial velocity was fitted by this function.

3.2.5 Exterior Ballistics

The theory of air drag experienced by bullets and shells is covered by the exterior ballistics. Air drag components and their calculation method for bullets and shells were introduced in Chapter 3 (Pu 1983). The three main components of the drag, namely friction drag, eddy drag and wave drag were elaborated one by one. For the practical purpose, the values of the key parameters in the calculation of some standard bullets were listed in tables.

Gao and Hu (Gao and Hu 1996) introduced the exterior ballistics theory to calculate the rock trajectory after blasting. The form of air drag force they use was $F(v) = a + bv^n$ (Pu 1985), here a, b and n were empirical coefficient. And the rock rebound was considered as well.

3.3 Adoption of equations of motion

When spinning motion is excluded, the translational motion of a flying object can be described by the motion of its centre. The forces acting on the object are the gravitational force and drag force only. The gravitational force acted on a debris mass m is constant and equal to mg, while the drag force F_d is varying and is proportional to the square of the velocity. The kinematic relationship between acceleration a, velocity V and position (x,y) can be expressed in differential equations. Hence, the equation of motion can be obtained by numerical integration of the differential equations (Tan, Frick et al. 1987) as follow.

$$V_x = \frac{dx}{dt} = V\cos\theta \tag{3.1 a}$$

$$V_y = \frac{dy}{dt} = V\sin\theta \tag{3.1 b}$$

$$a = \frac{dV}{dt} = -g\sin\theta - gkV^2 \tag{3.1 c}$$

$$\varphi = \frac{d\theta}{dt} = -g\frac{\cos\theta}{V} \tag{3.1 d}$$

Here, V is the velocity of the debris, θ is the slope of the trajectory to the horizontal, g is the acceleration due to gravity, x and y are the Cartesian coordinates of the debris. The basic parameters involved in the debris trajectory calculation are shown in the figure below.

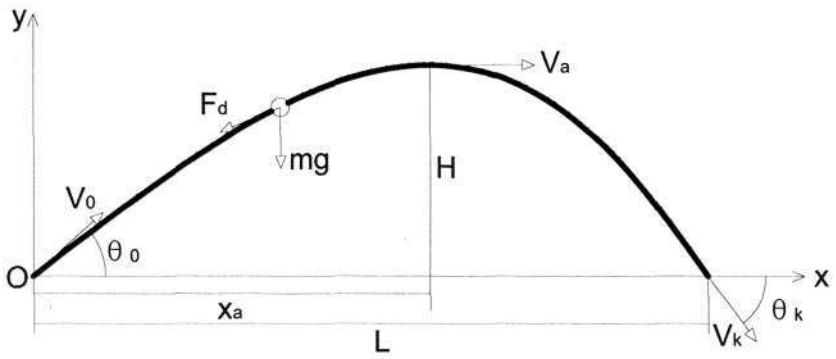

Fig. 3.1 Basic parameters of trajectory

Here, V_0 and θ_0 are the initial or the projective velocity and angle of the debris; V_k and θ_k are the landing velocity and angle when debris hits the ground; V_a and x_0 are the velocity and horizontal displacement when debris gets to the vertex of the trajectory; H is the vertex height; L is the debris horizontal displacement before it hits the ground.

The solution for Eqs (3.1), obtained by Euler's method, consists of an explicit analytical dependence of the velocity on the slope of the trajectory and three quadratures (Tan, Frick et al. 1987).

$$V(\theta)=\frac{V_0\cos\theta_0}{\cos\theta\sqrt{1+kV_0^2\cos^2\theta_0(f(\theta_0)-f(\theta))}} \tag{3.2 a}$$

where

$$f(\theta)=\frac{\sin\theta}{\cos^2\theta}+\ln tg\left(\frac{\theta}{2}+\frac{\pi}{4}\right) \tag{3.2 b}$$

$$x=x_0-\frac{1}{g}\int_{\theta_0}^{\theta}V^2d\theta \tag{3.3 a}$$

$$y=y_0-\frac{1}{g}\int_{\theta_0}^{\theta}V^2\tan\theta d\theta \tag{3.3 b}$$

$$t=t_0-\frac{1}{g}\int_{\theta_0}^{\theta}\frac{V}{\cos\theta}d\theta \tag{3.3 c}$$

Direct integration of the integrals in Eq.3.3 would be complicated. However, it can be approximated over a fairly small localized path interval [θ_0, θ] (e.g. 0.1°), and thus explicit form could be obtained by using 'quadratures by parts' as follow (Chudinov 2001).

$$t = t_0 + \frac{2(V_0 \sin\theta_0 - V \sin\theta)}{g(2+\varepsilon)} \tag{3.4 a}$$

$$x = x_0 + \frac{V_0^2 \sin 2\theta_0 - V \sin\theta}{2g(1+\varepsilon)} \tag{3.4 b}$$

$$y = y_0 + \frac{V_0^2 \sin^2\theta_0 - V^2 \sin^2\theta}{g(2+\varepsilon)} \tag{3.4 c}$$

$$\varepsilon = k(V_0^2 \sin\theta_0 + V^2 \sin\theta) \tag{3.4 d}$$

By dividing the trajectory path into a series of small intervals [θ_0, θ], the whole trajectory could be traced step by step. The velocity and position $V(\theta)$, $t(\theta)$, $x(\theta)$, $y(\theta)$ in each new step, j+1, could be derived from Eq.3.4 (e) with the initial values derived from previous step j. That is,

$$V_{0,j+1}=V(\theta_j), \quad t_{0,j+1}=t(\theta_j), \quad x_{0,j+1}=x(\theta_j), \quad y_{0,j+1}=y(\theta_j) \tag{3.4 e}$$

3.4 Summary

The research scope of this chapter is to find out the equations of motion for describing debris trajectory. By the review of the foregoing research and scientific judgment, the goal has been achieved.

Then code accounting for the debris trajectory in the C++ program is going to be compiled according to the adopted equations (3.4).

4. Drag force in the equations of motion

4.1 Overview

In this research, the debris motion only accounts for the gravitational and drag force. The gravity load of debris is remaining constant. It is easy to deal with as soon as the debris mass is obtained. While, the drag force is more complicated to consider. It is known that drag force F_d is related to lots of factors, such as the object's velocity, frontal area, shape, et al. The medium characteristic affects the drag force as well.

In this chapter, equation of drag force is concerned. The important parameter, debris drag coefficient C_d is discussed by details.

4.2 Review

4.2.1 Fluid dynamics

At first, the basic theory about fluid drag is concerned. '*Experiments show that any body placed in a moving stream experience drag. If a body moves relative to a still fluid, drag force resists the motion. The drag force vector always points downstream. Lift forces are not necessarily presents in all flows; they occur only if there is asymmetry.*' '*If the flow is completely asymmetric, either because the three-dimensional body has no plane of symmetry or because the approach flow is not parallel to the symmetry plane, the resultant force has three components, called drag, lift, and side force.*'(Gerhart, Gross et al. 1992)

'*As Reynolds number is the ratio of inertia force to viscous force in the fluid, it is reasonably assume that high Reynolds number flow is approximately inviscid.*' (Gerhart, Gross et al. 1992) If the body is blunt, the (high Reynolds number) drag is primarily form drag or pressure drag. If any analytical method is introduced to find out the debris drag coefficient, the friction drag is likely to be neglected, though except for several simple shapes, like parallel plate, analytically predicting drag coefficients with confidence is difficult.

4.2.2 Exterior ballistics

For the bullet placed with the axis coinciding with the speed vector in the wind tunnel, some of the investigation is as followed. When the relative speed between the medium and bullet is not so fast, as the air is non-ideal fluent and it is viscous gas, the drag force due to the internal friction of air is measured. This kind of the drag is called the *friction drag* (Pu 1983).

Friction drag arises from the friction of the fluid against the "skin" of the object that is moving through it. A boundary layer is that layer of fluid in the immediate vicinity of a bounding surface. For the continuously forming of the boundary layer near the bullet surface, the kinetic energy of bullet is transferring to the boundary layer. As a result, the bullet speed is slowed down. This is the cause of the friction drag.

When the speed is up to a specific value, the fluid become turbulent from laminar, the air viscosity increased a lot, which causes the average velocity of air in the boundary layer to increase and more kinetic energy of bullet is consumed accordingly. In addition, the friction drag is related to object surface roughness. The friction drag of bullet with rough surface is 2 to 3 times more than that of smooth one. In the sub-sonic speed range, friction drag takes up 35% to 40% of the whole drag force, while it is down to only 10% when the speed in super-sonic range.

If the air speed keeps on increasing, the airflow is separated from the rear part of bullet, which causes the vortexes to form at the same time. An obviously resistance force enlargement is measured. This kind of drag is called the *vortex drag*, whose

main cause is the pressure difference between the head and rear part of the object when the boundary layer is separated.

The two kinds of drag force mentioned before are both measured and discussed within the sub-sonic range. If the bullet is placed super-sonic wind-tunnel, besides the quantities of the vortexes at the rear part of the bullet, there is intensively impacted air layer to be discovered at both the head and rear part of the bullet, with the approximate cone shape. This is so-called the *shock wave* in aerodynamics. The air drag is increased intensively when the shock wave occurs.

4.2.3 C_d - Re relationship

The drag coefficient C_d is a number that aerodynamicists use to model all of the complex dependencies of shape, inclination, and flow conditions on moving object drag. This dimensionless value quantity the he drag or resistance of an object in a fluid environment such as air or water. The higher the C_d, the higher aerodynamic or hydrodynamic drag force the moving body will experience (Clancy 1975).

The two basic components contributing to the drag coefficient of any object are skin friction and form drag. When referring to the theory of exterior ballistics, they are the friction drag and vortex drag respectively. When the lift force occurs, the induced drag must be included. The drag coefficient of a complete structure such as an aircraft also includes the effects of interference drag (Abbott and Von Doenhoff 1959; Clancy 1975).

The drag coefficient is always associated with a particular surface area. It is a ratio between two numbers in the same units of area . For automobiles and many other objects, the reference area is the frontal area of the object (i.e., the cross-sectional area is the area perpendicular to the speed vector); this area tends to be small. For airfoils, the reference area is the square of the chord of the airfoil, which can be easily related to wing area. Since this tends to be a rather large area, the resulting drag coefficients tend to be low. So it gives a much slower drag coefficient than vehicles with the same drag. Airships and bodies of revolution use the volumetric drag coefficient, in which the reference area is the square of the cube root of the

airship volume. Submerged streamlined bodies use the wetted surface area (Fox and McDonald 1994).

The Reynolds number expresses the ratio of inertial (resistant to change or motion) forces to viscous (heavy and gluey) forces. This dimensionless number is used to characterize different flow regimes, such as laminar or turbulent flow: laminar flow occurs at low Reynolds numbers, where viscous forces are dominant, and is characterized by smooth, constant fluid motion, while turbulent flow occurs at high Reynolds numbers and is dominated by inertial forces, which tend to produce random eddies, vortices and other flow fluctuations(Munson, Young et al. 2002).

The value of drag coefficient C_d is a function of the shape of object and also the Reynolds number (Re). The dimensionless number Re is defined as follows:

$$\mathrm{Re} = \frac{\rho l v}{\eta} \tag{4.1}$$

where l represents the characteristic length scale of the object in the cross-sectional plane (in the case of a sphere, this is just the diameter 2R) and η the dynamic viscosity of the medium.

The solid line in Fig. 4.1 shows the typical relationship between the drag coefficient C_d and the Reynolds number Re (Hoerner 1965) for a sphere. As can seen from the figure, C_d is less than 1 when Re is greater than 10^2; and C_d is about 0.5 when Re lies in the interval [10^3 , 3×10^5]. The sudden drop of C_d, when Re is about 4×10^5, is due to the drag crisis. Then C_d is rises up gradually.

The dashed line in Fig. 4.1 shows relationship between C_d and Re for a circular disk. This shape is so popular because its drag coefficient C_d is nearly constant across all operating conditions like Reynolds number. Above a Reynolds number of 1000, the drag coefficient of the circular disk becomes a constant that has been consistently measured as 1.17.

While the dashed line in Fig. 4.2 shows relationship between C_d and Re for a circular cylinder in the flow normal to the axis. C_d is almost constant, equaling to

1.2, in the interval [10^3, 3×10^5]. The sudden drop of C_d occurs at the same Re interval as the sphere does. As a overall comparison, C_d of cylinder is higher than that of sphere when Re is greater than 2×10^1.

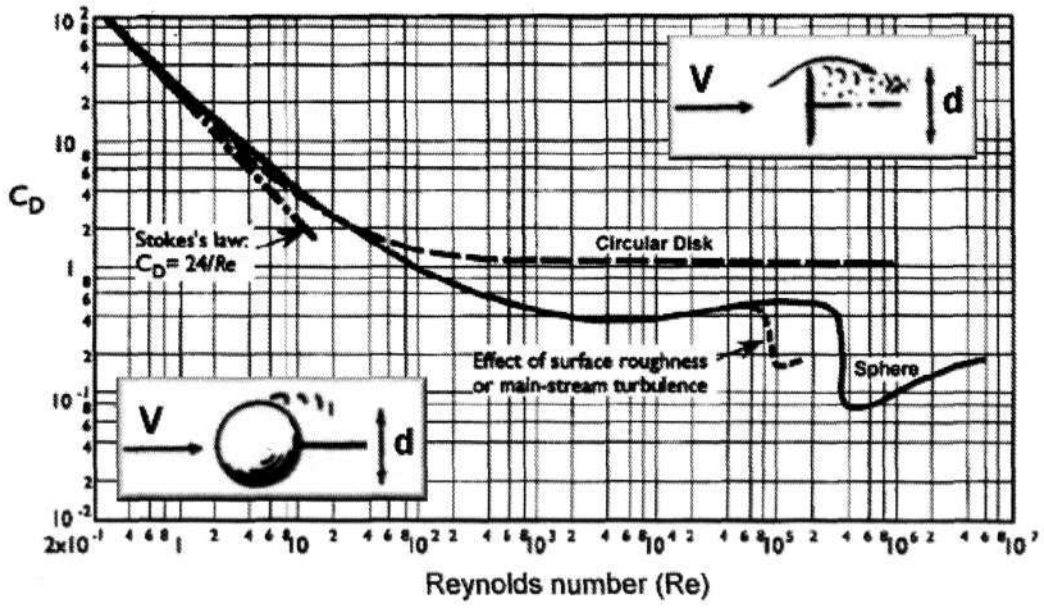

Fig. 4.1 Drag coefficient of a circular disk and a sphere versus Reynolds number

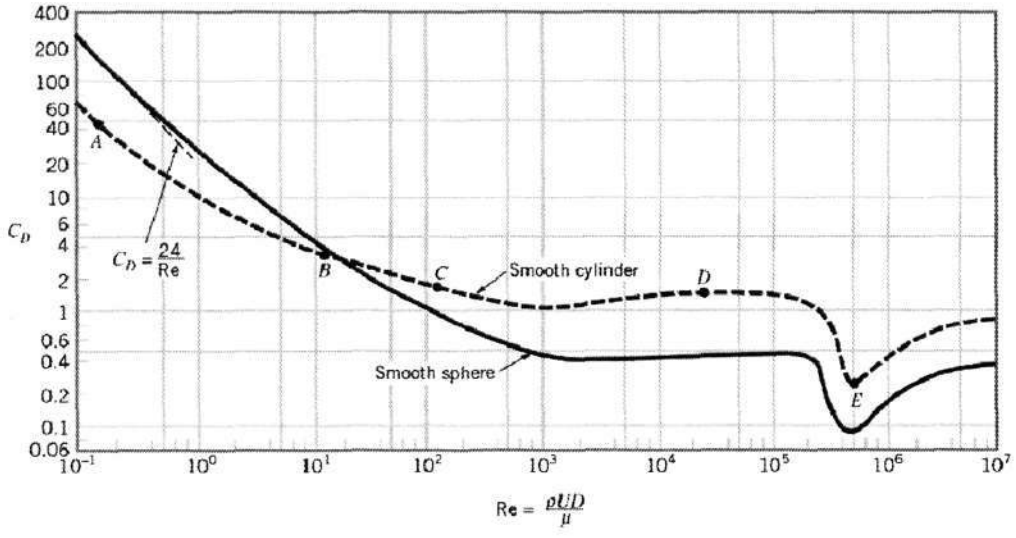

Fig. 4.2 Drag coefficient of the circular cylinder in a flow normal to the axis and a sphere versus Reynolds number

4.2.4 C_d at high Reynolds number and drag crisis

It can be observed from the Fig. 4.3 (Nakamura and Tomonari 1982) easily that there is he sudden drop in C_d, both of the sphere and cylinder, at a very high Re value, about 2.5×10^5. This phenomenon is the so-called drag crisis.

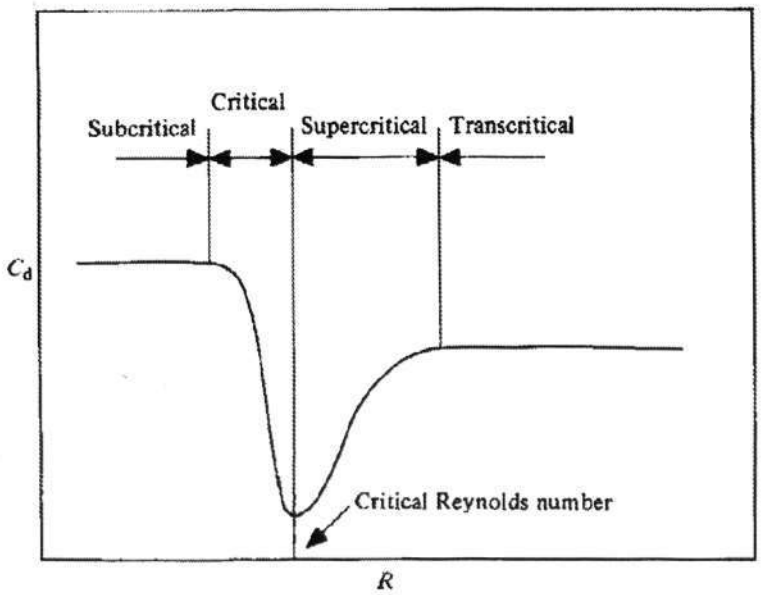

Fig. 4.3 Four Reynolds number ranges

The four different high-Reynolds-number flow ranges are referred to as the subcritical, the critical, the supercritical, and the transcritical, with the critical Reynolds number being identified as that giving the minimum C_d (Farell 1981) .

Each of these ranges has its own characters according to its special boundary layer behavior. Subcritical gets the purely laminar separation; in the critical range, the laminar bubbles are followed by turbulent reattachment and delayed final separation; in the supercritical range, the transition is ahead of separation and is moving upstream; in the transcritical range, the transition is sufficiently close to the stagnation point that the flow becomes independent of Re.

If the drag coefficient is measured for the cylinders with different kinds of roughness, that the earlier transition to the critical is observed, thereby accompanying an increase in the minimum C_d. The roughness is measured by the roughness height to cylinders diameter ratio r/D.

The three fitting curves with notations, square, cross and hollow triangle are the measured results for the drag coefficients corresponding to three larger roughnesses, up to 10^{-2}. Then they are approaching a common level in the transcritical range, indicated by Fig. 4.4 (Nakamura and Tomonari 1982). While curve with the black circles presents the experiment results for the smooth cylinder as comparison.

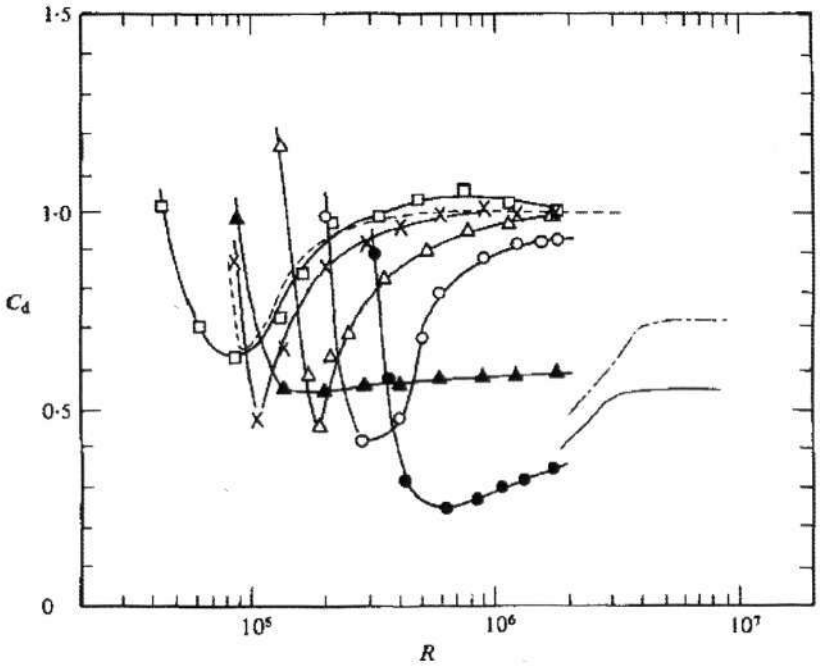

Fig. 4.4 Drag coefficient of cylinders with different roughnesses

4.3 Drag force

The general equation for the drag force is(Fox and McDonald 1994):

$$F_d = \frac{1}{2} C_d \rho_a A v^2 \tag{4.2}$$

where C_d is drag coefficient, ρ_a is density of the medium surrounding the flying object, v is velocity of the flying object, A is the object's cross-sectional area. In this study, A is defined as debris' maximum sectional area perpendicularity to the motion direction. The equation means that the drag force is proportional to the drag coefficient, the air density, the normal sectional area, and the square of the velocity.

In the following, a new parameter k is introduced, and the equation of motion is re-written as,

$$F_d = mgkv^2 \tag{4.3}$$

where

$$k = \frac{\rho_a A}{2mg} C_d \tag{4.4}$$

As the shape of a fragment will never be a perfect square or a rounded sphere, an equivalent cross-sectional area is derived from an equivalent cube as follow, where volume is the volume of the fragment.

$$A = volume^{2/3} \tag{4.5}$$

The density of air is assumed constant, equaingl to 1.293kg/m^3. The drag coefficient C_d will be further elaborated in Section 4.4.

4.4 Determination of drag coefficient C_d

To describe the debris free flying motion, it is necessary to assess its range of *Re*. The air density ρ is assumed to be constant, ρ=1.293 Kg/m^3. So is the viscosity of air (use the value η=1.78×10^{-5} kg/(m·s) at 15°C). As such, the Reynolds number will be proportional to the characteristic size of debris (l) and the velocity (v). To estimate the lower bound of *Re*, set l_1 = 0.01m and v_1 = 10 m/s; while for the upper bound, set l_2 = 0.20 m and v_2 = 500 m/s. Thus

$$\mathrm{Re}_{lower} = \frac{\rho l_1 v_1}{\eta} = \frac{1.293 \times 0.01 \times 10}{1.78 \times 10^{-5}} \approx 7.3 \times 10^3$$

$$\mathrm{Re}_{upper} = \frac{\rho l_2 v_2}{\eta} = \frac{1.293 \times 0.20 \times 500}{1.78 \times 10^{-5}} \approx 7.3 \times 10^6$$

This estimated range is covered by the rectangular shadow in Fig. 4.5, shown below.

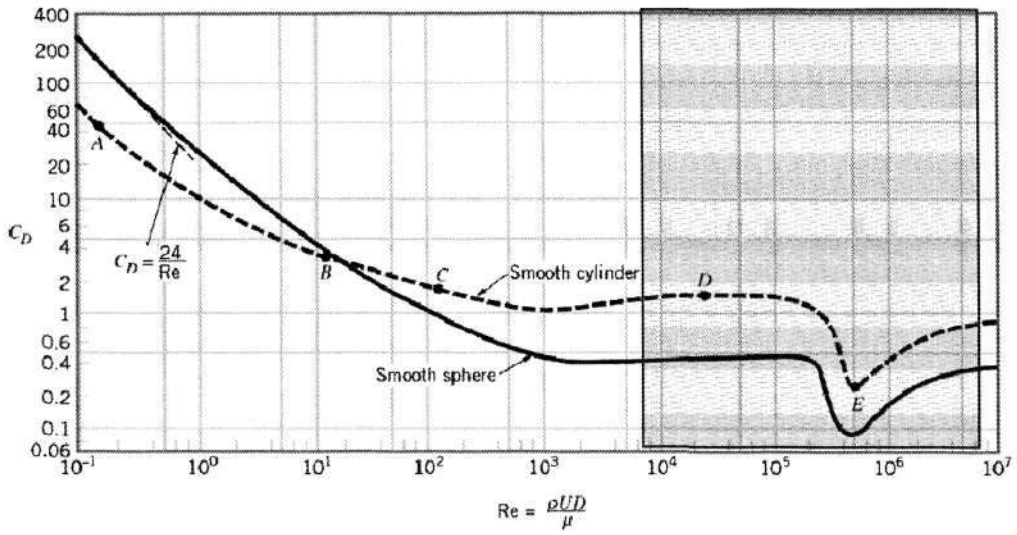

Fig. 4.5 Estimated *Re* Range for debris

Note that the relationship shown in Fig. 4.1 and Fig. 4.2 between Reynolds number *Re* and the drag coefficient C_d is for a perfect sphere and cylinder with smooth surface where the friction drag is relatively small. In the current study, the debris has highly-irregular rough surface which causes much higher friction drag than the smooth spherical surface. Though no systematic experimental investigation were carried out for the C_d-*Re* relationship for the rough-surfaced debris, it is observed from tests of cylinder with various roughnesses that the rough surface causes the drag crisis shift to a smaller *Re* interval, accompanying the increase of the minimum C_d. (this phenomenon is shown in Fig. 4.4)

Apart from this, the shape of the cylinders affects on the drag coefficient and drag crisis. Seen from Fig. 4.6, the square cylinder has overall drag coefficient higher than the circular one (Barr and Barnaud 1995). Further, the square cylinder totally skips the drag crisis.

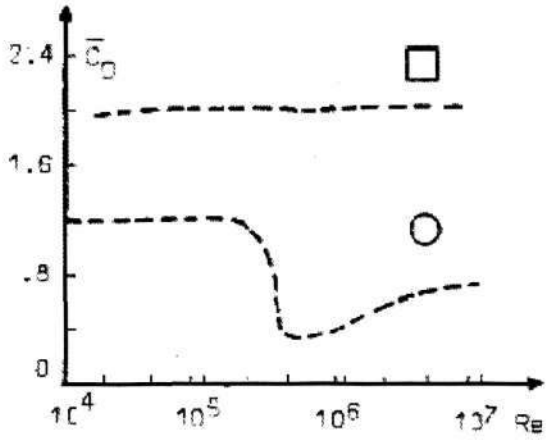

Fig. 4.6 Influence of the shape on the drag coefficient of circular and square cylinders

According to foregoing analysis, it is reasonable to assume that the drag coefficient for the debris remains more or less constant against the Reynolds number up to the value of as such, the drag coefficient C_d falls within the range [0.5, 1] for Reynolds number between Re_{lower} and Re_{upper}.

To adopt a reasonable value for the rough-surfaced debris, values for three benchmark shapes or surfaces are considered as shown in Table 4.1 Drag coefficient C_d of different shapes below (Lee 1974).

Table 4.1 Drag coefficient C_d of different shapes

OBJECT	C_d	REYNOLDS NO. RANGE	CHARACTERISTIC LENGTH	CHARACTERISTIC AREA
SPHERE 	$24 (N_R)^{-1/2}$	$N_R < 1$	d	PROJECTED AREA
	0.47	$10^3 < N_R < 3 \times 10^5$		
	0.2	$N_R > 3 \times 10^5$		
CIRCULAR CYLINDER 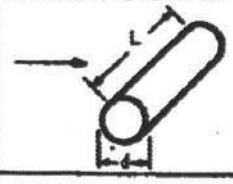	L/d 1 0.63 5 0.8 10 0.83 20 0.93 30 1.0 ∞ 1.2	$10^3 < N_R < 10^5$	d	PROJECTED AREA
SQUARE CYLINDER 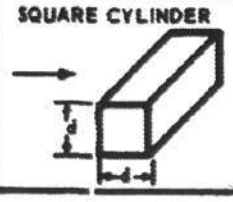	2.0	$3.5 (10)^4$	d	PROJECTED AREA

The values for the spherical shape are in generally the smallest, while the values for the circular and square cylinders are higher. fall within the range [~0.7, 2.0]. Consider the value C_d =0.7 for a circular cylinder having aspect ratio (L/D) of 2, and the value C_d =2.0 for a square cylinder of any aspect ratio. As the debris shape will never be a perfect smooth circular cylinder but multi-angular, it makes sense to assume that the drag coefficient for debris is closer to that for the square cylinder, whose value is independent of aspect ratio (L/D). Again, the multi-angular shape of debris is somehow between the circular and the square. It has the transitional shapes from the smooth circular (C_d =0.7) to the blunt square (C_d =2.0). In the absence of experimental data, values of drag coefficient for the intermediate shapes are assumed. The octagonal shape is assumed 1.2; while the hexagonal is 1.6 as shown in Fig. 4.7. In next section, drag coefficients of 1.2, 1.6 and 2.0 are used, and their effects on the debris trajectory are investigated.

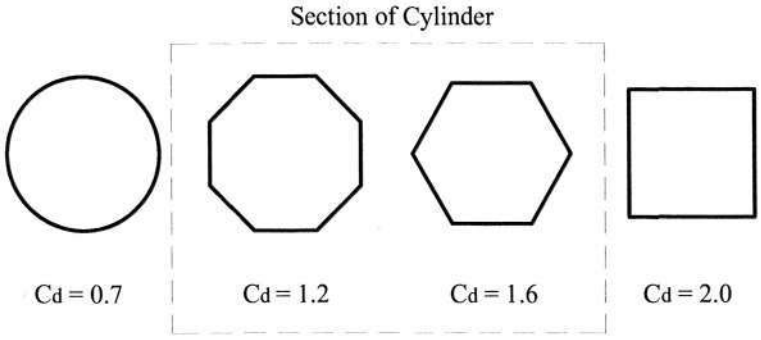

Fig. 4.7 Drag coefficient of different cylinders

4.5 Effects of C_d on debris trajectory

To investigate the effects of the value of drag coefficient C_d on the trajectory, a fragment (of a single element size) is used. The debris with the mass of 0.2 kg has an ejecting velocity of 100 m/s at an angle 5° with the horizon. Fig. 4.8(a) shows the effect of C_d on the of debris' travel distance. Fig. 4.8 (b) shows the effect on the final velocity v_K when the debris hits the ground. For easy visualization, trajectories generated by adopting different values of C_d are shown in Fig. 4.9. It can be seen that value of C_d has significantly effect on the debris travel distance, and it is more prominent when C_d is less than 1.0. For the range ($1.2 < C_d < 2.0$) of current interest, the travel distance for the higher one (C_d =1.2) is about 177m; while the lower one (C_d =2.0) is about121m, which is approximately 68% of 177m.

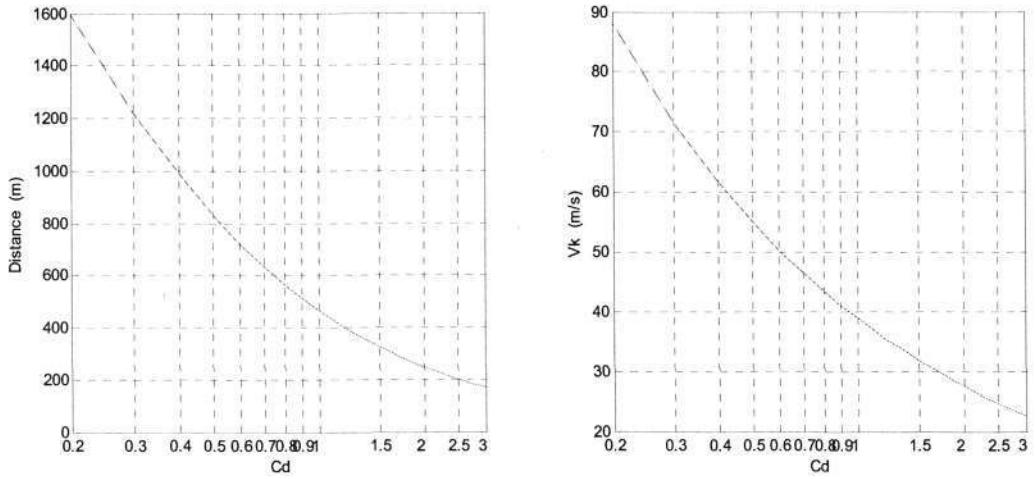

(a) Debris' travel distance **(b) Debris' final velocity v_k**

Fig. 4.8 Effects C_d of on debris traveling distance and landing velocity

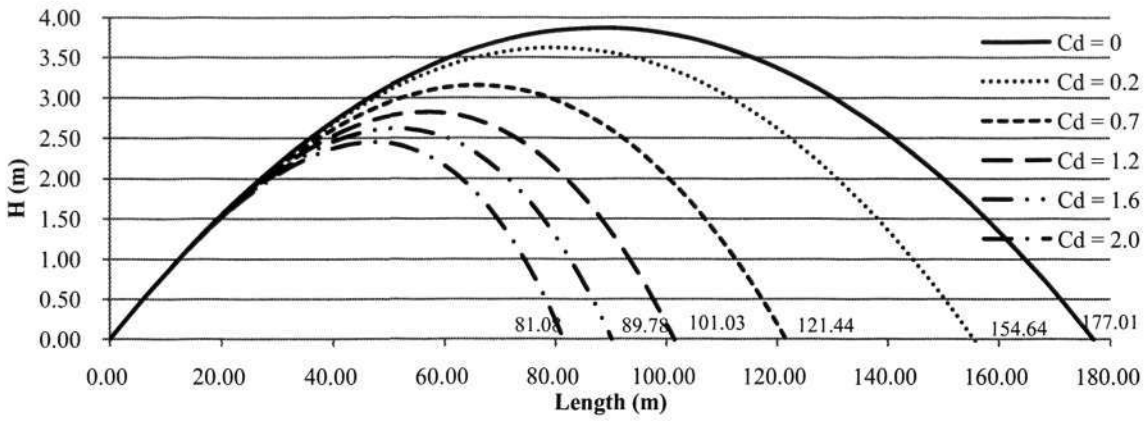

Fig. 4.9 Debris trajectory of various C_d (m = 0.2 kg, V_0 = 100 m/s, θ_0 = 5°)

4.6 Summary

In this chapter, the debris drag force in equations of motion was discussed. The drag force equation has been chosen and the assumptions for applying the equation in simplified calculation have been made.

The drag coefficient range was determined by scientific hypothesis based on the foregoing research. Finally the C_d range of [1.2, 2.0] was determined for the

calculation in this thesis. The effects on the debris trajectory due to drag coefficient were observed last.

5. Blast debris simulation algorithm

5.1 Overview

The whole blast debris simulation is divided into two main parts. One is the break-up process and the other one is debris throw. In this chapter, the algorithms involved in both simulation parts are introduced. Details are given to the algorithm defining the debris. The validity of the debris simulation is discussed as well.

5.2 Break-up simulation algorithm

The formation of debris is a process of crack initializing and developing. Because of the difficulties in locating the crack initializing and determining the crack developing directions, it is critical to realistically model the physical phenomenon. In LS-DYNA, there are two algorithms to achieve the goal. As both the two algorithms get advantages and disadvantages, which are redeemed mutually, the two algorithms are employed simultaneously to model the break-up of the structure in this thesis. The details on algorithm are given below.

5.2.1 Element erosion algorithm

Element erosion algorithm is implemented by adding erosion criteria to a given material element.(Lu, Gong et al. 2005; Yu Q.J., Yang Y.W. et al. 2008) These criterias include pressure, stress, strain, damage value and other measure parameters. Once a specified term in an element reaches a given critical value, the element is then removed from the computation and fracture occurs. For instance of the principle strain used in the thesis, the failure criterion can be given as

$$\varepsilon_{1i} \geq \varepsilon_{\max} \tag{5.1}$$

where ε_{1i} is the maximum principal strain of any element i, and ε_{max} is the principal strain at failure, normally positive as tension strain.

In LS-DYNA, the time step corresponds to the acoustic wave passing through the shortest characteristics length. As the element undergoes deformation, the characteristics length gets smaller and this translates to a smaller time step. In certain instances, such characteristics length becomes too small and singularity problem could result. To improve the computational efficiency and avoid singularity problem, a minimum time step is introduced. The minimum time step criterion uses a reduction factor Δ_R on the initial time step size to determine a minimum time step size Δt_{min}. Once the current time-step size of any element is smaller than Δt_{min}, the element will be eroded from the structure and no longer take part in the computation (LS-DYNA 2003). Once an element is eroded, it is regarded as a rigid body with constant velocity and is invisible in the post-processing.

5.2.2 Constrained tied nodes with failure/nodal splitting algorithm

An alternative method is the "Constrained tied nodes with failure" algorithm in LS-DYNA (LS-DYNA 2003). This algorithm characterizes that elements are discrete but continuous in space with all nodes at one coincided location constrained to be tied together. Namely, there are no shared nodes between two neighboring elements; the connection between neighboring elements is established by fixed constraints between nodes that will break or split to form fracture while the volume weighted plastic strain of a constrained nodal set ($\varepsilon^p{}_{cns}$) reaches a certain failure plastic strain specified($\varepsilon^p{}_{max}$). So the failure criterion of the constrained nodal set given is expressed as:

$$\varepsilon_{cns}^{p} = \left(\frac{\sum_{i=1}^{n} V_{ne,i} \varepsilon_{ne,i}^{p}}{\sum_{i=1}^{n} V_{ne,i}} \right) \geq \varepsilon_{\max}^{p} \tag{5.2}$$

where $V_{ne,i}$ and $\varepsilon^{p}{}_{ne,i}$ are, respectively, the volume and plastic strain of element i related to the nodal set given.

5.2.3 Combination of the two algorithms with three failure criteria

To simulate the concrete structure breakup under intense blast loading, the element erosion algorithm and the tied nodal splitting algorithm are combined. The element erosion technique is mainly used to control an appropriate time-step size by removing singular elements through setting appropriate values for tension failure strain ε_{max} and a time-step size reduction factor. The initialization and development of cracks and formation of debris are mainly by the tied nodes splitting algorithm through a small nodal plastic strain $\varepsilon^{p}{}_{max}$ at failure.

Here, the critical nodal tensile strain is set to 0.05 and the erosion strain at 1.2 for concrete and 0.05 for soil.

5.3 Defining debris

This section explains the algorithm to define the debris from the LS-DYNA output. Explanation from the programming point of view is give as well. After the debris defining, the debris initial conditions, such as the ejection position, velocity and angle are defined accordingly.

5.3.1 Managing the nodal and element information

The nodes information of each element in the structure is grafted from the LS-DYNA output file named *KNE*.

At the start, the program is coded to reads the nodal information, including coordinates and their ID number. Every eight successive nodes are assigned to an element, which does not share the same nodal name/number with other elements regardless of being at the same location. Each element possesses their independent nodes. Once the elements are constructed, element center point and volume are

calculated from their nodal coordinates. Element mass is obtained after the density of the material is decided.

All the structural element information is stored in an array in five sequential sub-arrays according to their position in the real structure, which is divided into five rectangular plates – the roof slab and the four walls. For the simulation in this thesis, the magazine is divided into five parts, as No.0 Top, No.1 Back, No.2 Right, No.3 Front-small and No.4 Front-large.

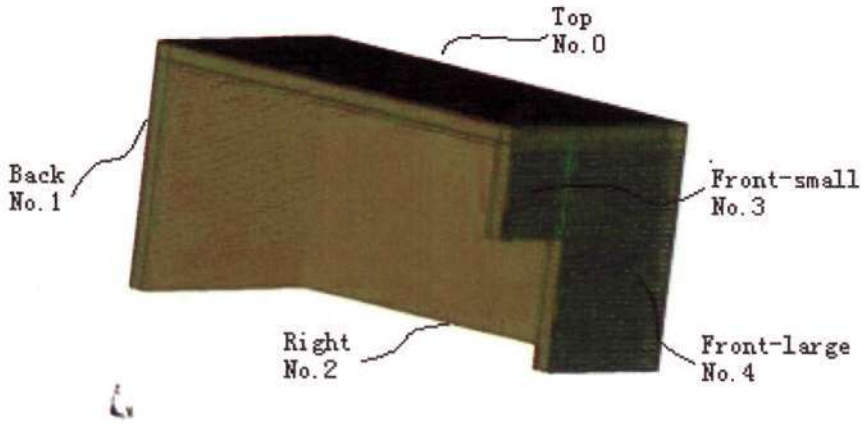

Fig. 5.1 Magazine decomposition

The elements are assigned an ID number consisting of the plate's sequential number and its address in that sequence. Then, the code will sort out the six adjacent elements for each element, and the connecting nodes between elements. In terms of coding terminology, 'pointers' are used to identify the addresses of all this information stored in the computer memory arrays.

Nodal information and element information are stored in two separate classes. In the programming code, the nodes and the center points of element are defined as a point class. For each point class, the global nodal coordinates and the nodal ID number are stored. In the same way, element class is to store the information of element. The 8 nodal ID numbers of each element and their pointers, element ID number, element volume and mass, element connection and an element erosion-related value are all stored under the element class.

5.3.2 Debris formation algorithm

5.3.2.1 Element displacement and velocity after break-up

The information on displacement and velocity of all nodes during break-up process is stored in the output file named *NODOUT* in sequence of intervals Δt_s. Thus for a given time t, the displacement u^{ECt} and velocity v^{ECt} of an element center is the average value of its 8 corner nodes, which are represented as

$$u^{\mathrm{EC}t} = \frac{1}{8}\sum_{i=1}^{8} u_i^t \tag{5.3}$$

$$v^{\mathrm{EC}t} = \frac{1}{8}\sum_{i=1}^{8} v_i^t \tag{5.4}$$

where u_i and v_i are the displacement and velocity of the i^{th} node in this element at time t.

5.3.2.2 Debris definition from the recovered eroded- element pool

From the information recorded in the file named *MSSG* for the eroded elements, the element number and its erosion time can be retrieved. The index set of erosion elements are represented by Φ^{EE}. All the eroded elements in the record will be grouped according to the sequence of time intervals. G_j^{EE} and t_j^{GE} are, respectively, the j^{th} eroded element group and its erosion time.

$$\phi^{\mathrm{EE}} = \left\{ i \middle| \text{Ele } i \text{ has eroded, } i=1, 2, \cdots, N^{\mathrm{TE}} \right\} \tag{5.5}$$

$$G_j^{\mathrm{EE}} = \left\{ i \middle| t_i^{\mathrm{EE}} - t_j^{\mathrm{GE}} \le \Delta t^{\mathrm{GE}}, i \in \phi^{\mathrm{EE}} \text{ and } i = 1, 2, \cdots, N^{\mathrm{TE}} \right\} \tag{5.6}$$

$$\begin{cases} t_1^{\mathrm{GE}} = \min\left(t_i^{EE}\right) \middle| i \in \phi^{\mathrm{EE}} \text{ and } i = 1, 2, \cdots, N^{\mathrm{TE}} \\ t_j^{\mathrm{GE}} = \min\left(t_i^{EE}\right) \middle| t_i^{\mathrm{EE}} > t_{j-1}^{\mathrm{GE}} + \Delta t^{\mathrm{GE}}, i \in \phi^{\mathrm{EE}} \text{ and } i = 1, 2, \cdots, N^{\mathrm{TE}} \end{cases} \tag{5.7}$$

where t_i^{EE} is the erosion time of element i, Δt^{GE} is a specified interval.

Note that the recorded erosion time of one element actually may not be the same as its physical break-up time.

For each eroded element group, we can obtain the number and size of debris through checking initial inter-element connection. Consequently, debris can be defined from the eroded-element pool.

5.3.2.3 Debris definition from the un-eroded-element pool

For un-eroded elements, the current distance of any nodal pair, which is at the same location but tied over the interface between two neighboring elements in the initial state, can be obtained from the results of last time step. If the distance is greater than a specified maximum distance $d_{\max}^{cpp}$, the pair of nodes splits (i.e., the constrained nodes tie between the two nodes is released). Note that two neighboring elements may still tie together if only one of their four nodal pairs splits (or separates) (i.e., not the whole interface between the two elements is fracture). If fracture does occur, the two neighboring elements separate. Thereby for a given element, one can loop through its surfaces to obtain an initial fragment. Upon repeatedly looping and checking the current disconnection of all tied nodal pairs along the outer surface of a sub-region, the possible formation of a piece of debris can be identified, and eventually a final form of fragment (or debris) is obtained when no other elements are tied to it. By treating the un-eroded elements in this way, we can define the sizes of fragments (or debris), formed from the mass of un-eroded elements.

5.3.2.4 Effects of Δt^{GE} and d_{max}^{cpp} on number and size of debris

After initial break-up, debris are defined from the eroded-element pool and the un-eroded element pool according to the two criteria, namely Δt^{GE} and $d_{\max}^{cpp}$. It is found that Δt^{GE} controls the number and size of debris formed from the eroded-element pool; whereas $d_{\max}^{cpp}$ controls the number and size of debris formed from the un-eroded-element pool. Δt^{GE} = 0.1 ms and $d_{\max}^{cpp}$ = 2 mm are adopted in the debris formation processes according to the previous research (Fan, Yang et al. 2007).

5.3.2.5 Debris ejection position and ejection velocity

Once the sizes of debris are defined, other physical and kinetic properties of debris can be derived from the information of its component elements. An individual debris' initial center $P^{FC}(x, y, z)$, mass M^F, volume V^F, displacement u^{FCt} and velocity can be defined as follow.

$$P^{\mathrm{FC}}(x,y,z)=\frac{1}{n^{\mathrm{FE}}}\sum_{i=1}^{n^{\mathrm{FE}}}P_i^{\mathrm{EC}}(x,y,z) \tag{5.8}$$

$$V^{\mathrm{F}}=\sum_{i=1}^{n^{\mathrm{FE}}}V_i^{\mathrm{E}} \tag{5.9}$$

$$M^{\mathrm{F}}=\sum_{i=1}^{n^{\mathrm{FE}}}\rho_i^{\mathrm{E}}V_i^{\mathrm{E}} \tag{5.10}$$

in which, $P_i^{EC}(x, y, z)$, V_i^E, and ρ_i^E, respectively, represents the initial center, volume and medium density of the i^{th} element in the fragment including n^{FE} elements. For 3D solid brick elements used in this computation, the initial center of any element is given as

$$P^{\mathrm{EC}}(x,y,z)=\frac{1}{8}\sum_{i=1}^{8}P_i(x,y,z) \tag{5.11}$$

where $P_i(x, y, z)$ is the coordinates of the i^{th} node in the element.

Considering an single debris, it is reasonable to evaluate its value at the centre by taking the arithmetical mean of values from all its component elements. The values of central displacement u^{FCt} and velocity v^{FCt} are defined as follow.

$$u^{\mathrm{FC}t}=\frac{1}{n^{\mathrm{FE}}}\sum_{i=1}^{n^{\mathrm{FE}}}u_i^{\mathrm{EC}t} \tag{5.12a}$$

$$v^{\mathrm{FC}t}=\frac{1}{n^{\mathrm{FE}}}\sum_{i=1}^{n^{\mathrm{FE}}}v_i^{\mathrm{EC}t} \tag{5.12b}$$

By summing up the initial position and the displacements u^{FCt} in all time steps, from the initial till the last time step, one can get the final position of an individual fragment, and it is its ejection position. Similarly, one can get the ejection velocity for an individual fragment. These two values are taken as the initial conditions in debris free-flying motion.

5.4 Validity of debris simulation

A RC box break-up simulation, which has been carried out according to the algorithm presented before, was compared to the Kasun II test No. 5 (Berglund, Carlberg et al. 2006) test results. The debris simulation has been verified by the comparison.

Internal dimensions of the RC cubic box were 2.0m × 2.0m × 2.0m. The charge weight was 160kg equivalent TNT with a loading density of 20kg/m^3.

5.4.1 Validity of structure break-up simulation

The response of the tested structure is captured via a high speed video and its response versus time was compared with the quarter simulation results, as shown in Fig. 5.2.

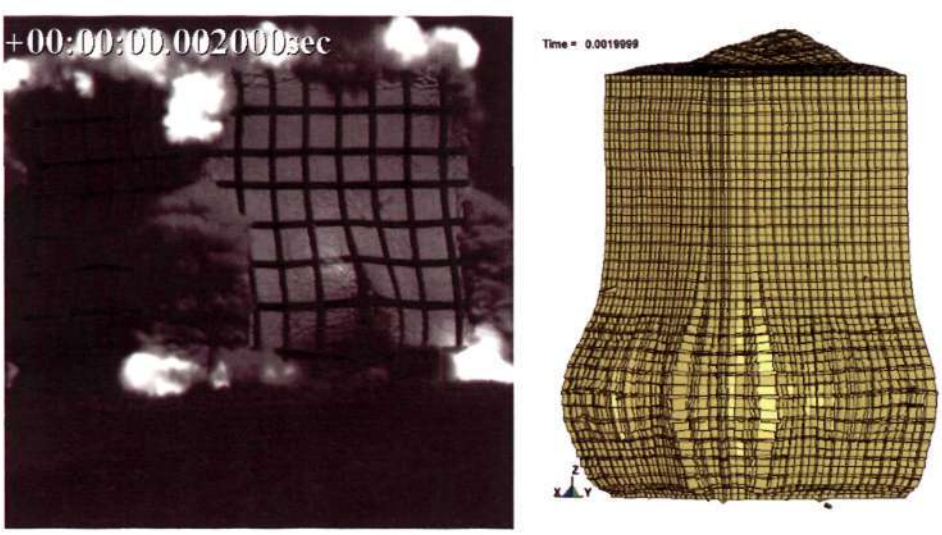

(a) at 2 ms

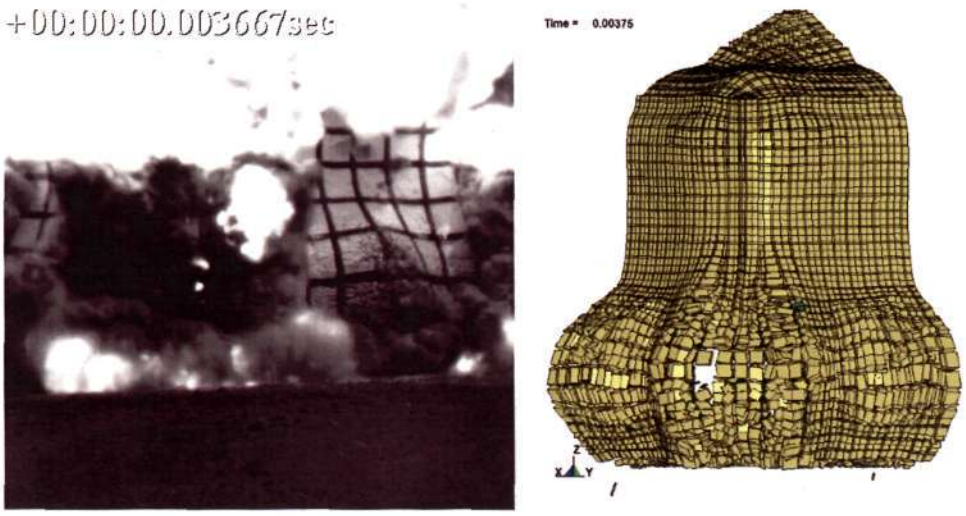

(b) at 3.67ms

Fig. 5.2 Test and numerical results of an RC structural break-up pattern for Kasun II Test 5

Observed from the simulation process, the formation pattern of the bulge, which was first at the side wall followed by the wall connection, as well as the crack location were in similarity with field test record. In the nutshell, the simulation was able to reproduce the blast process to some extent. Then the break-up simulation scheme has been verified.

5.4.2 Validity of debris throw simulation

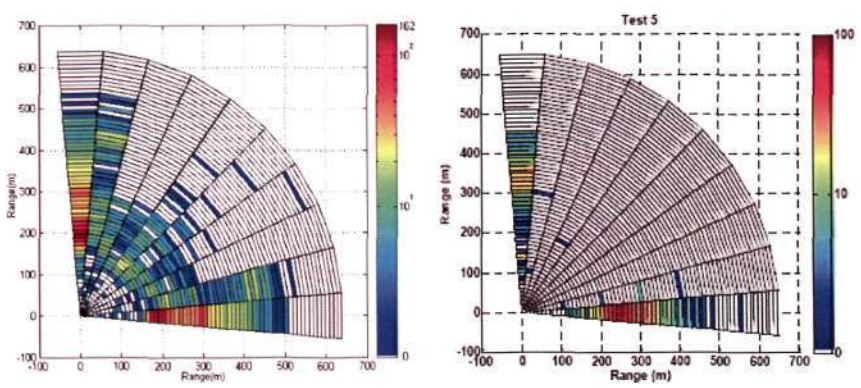

(a) Simulation **(b) Test**

Fig. 5.3 Comparison of debris dispersion pattern for Kasun II Test 5

Fig. 5.3 gives the comparison of debris scattering pattern of Kasun II Test 5 to the simulated one.

High debris distribution in the direction normal to the walls were found in test and simulated results. The simulated scattering pattern matches quite well with the test one. Then the debris throw scheme has been verified.

5.5 Summary

In this chapter, the algorithms employed to simulate the break-up process were presented first. A combined algorithm overcoming disadvantages and inheriting the advantages was adopted in calculation.

As the debris throw was modeled in C++ program, the re-arrangement of the debris information, which was derived from LS-DYNA output, is necessary. Then debris defining was carried out according to the related algorithms.

The validity of the debris simulation was given at last.

6. Debris simulation and results

6.1 Overview

In order to study the structural overall deformation, crack formation, debris and fragment formation, and final hazardous debris distribution under internal detonation, a full coupled 3-D numerical model for a typical box-shape Earth-Covered Magazine (ECM) is set up.

The magazine parameters are introduced at first. Then the simulation model in LS-DYNA is built up according to them. The magazine break-up pattern under high loading density and deformation pattern under low loading density are presented. Results of debris throw are discussed with details at last.

6.2 Simulation model

6.2.1 Magazine parameters

The reinforced concrete box (2% reinforcement magazine) has the following features and dimensions:

- Interior dimensions: 10.0m (Length, X direction), 10.0m (Width, Y direction), 5.0m (Height, Z direction);

- Wall and roof thickness: 0.5m, uniform;

- Door dimensions: 4m (Width, Y direction), 3m (Height, Z direction);

- Reinforced steel distributed at 0.14m space in two directions and double layers;

- Reinforced steel section: Ø32mm;

- Soil cover thickness: 0.6m.

6.2.2 Model set-up

The finite element model is built according to the foregoing dimensions and features. Because of symmetry, only half structure is built and the symmetry plane locates at the X-Z plane as can be seen in Fig. 6.1. For simplification, the door is replaced by a vent.

Fluid-solid interaction method (named Penalty Coupling in LS-DYNA) is employed to handle the interaction between explosion production and RC box, (Lu Y., Tu Z.G. et al. 2006). Lagrangian element is used to model the solids, while Eulerian is used for the air and TNT. Gravity load of soil cover is applied via the *load_body_z command.

To allow a direct comparison, the same concrete box-shape structure without and with earth cover are analyzed under comparable loading conditions. The study includes two charge stack formats, namely centered and distributed, as well as two loading density, namely 2.5 kg/m^3 and 30 kg/m^3. Thus, there are 8 different simulation cases. The cases are defined as AGM-C-30, ECM-C-30, AGM-D-30, ECM-D-30, AGM-C-2.5, ECM-C-2.5, AGM-D-2.5 and ECM-D-2.5, where AGM (Above Ground Magazine) and ECM (Earth Covered Magazine) refer to magazines without and with soil covered, C and D refer to Centered and Distributed charge stack formats, 2.5 and 30 refer to loading densities.

The whole model configuration under high loading density 30 kg/m^3 is shown in Fig. 6.1. The model configuration under low loading density 2.5 kg/m^3 is similar. Fig. 6.1(a) and (b) depict the centered stack case and Fig. 6.1(c) and (d) depict the distributed stack case.

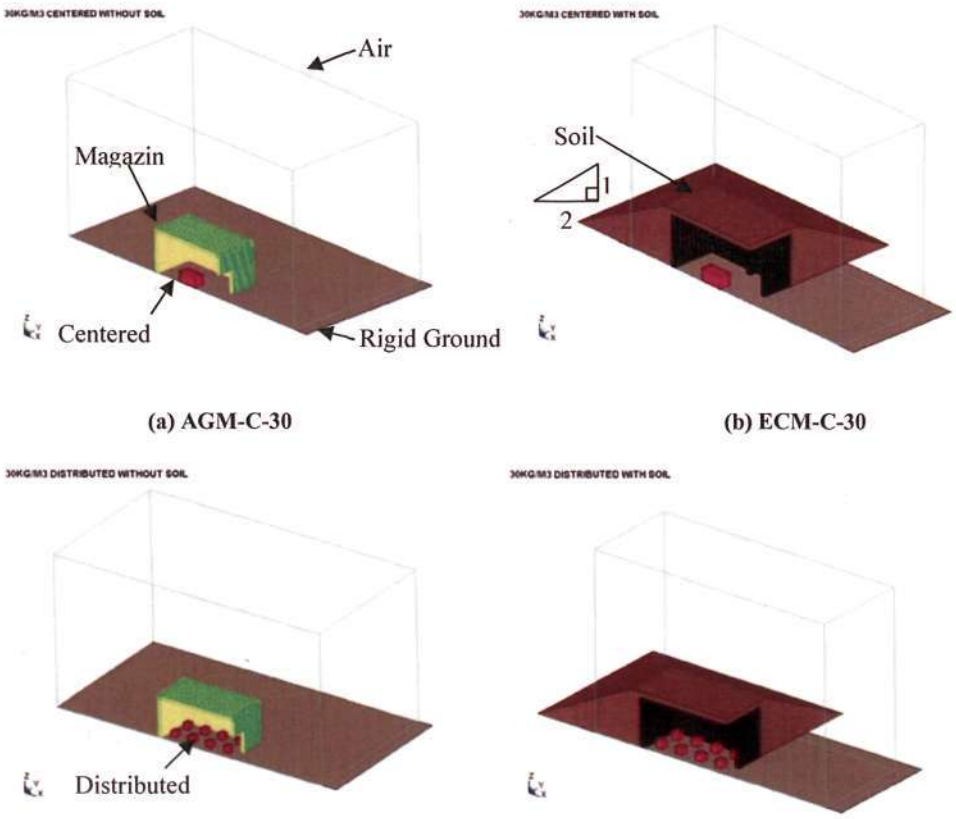

(a) AGM-C-30 **(b) ECM-C-30**

(c) AGM-D-30 **(d) ECM-D-30**

Fig. 6.1 Sketches of four cases at high loading density

6.2.3 Model mesh

Fig. 6.2 gives the mesh scheme used in this study and all parts are meshed by hexahedron elements. Fig. 6.2 (a) and (c) give the overall mesh on the symmetry plane respectively for ECM-C-30 and ECM-D-30. Fig. 6.2 (b) presents the local mesh of ECM-C-30 and Fig. 6.2 (d) presents the local mesh of ECM-D-30 on the section plane Y=1.25m.

It can be seen from these two local mesh figures that for the Eulerian mesh, TNT part is meshed by finer mesh and air part by coarser mesh. More details about the mesh schemes of Eulerian part can be found in Fig. 6.2 and Table 6.1.

Fig. 6.2 (e) and (f) give the mesh for RC box and soil cover respectively. The RC box (magazine) is meshed into 218,834 uniform 71mm^3 cubic elements including

33,384 Mix156 elements, 14,968 Mix321 (as described in Section 6.2.4) elements and 170,482 plane concrete elements. Soil cover is meshed by 681,840 hexahedron elements, which are finer in the region near to the RC box.

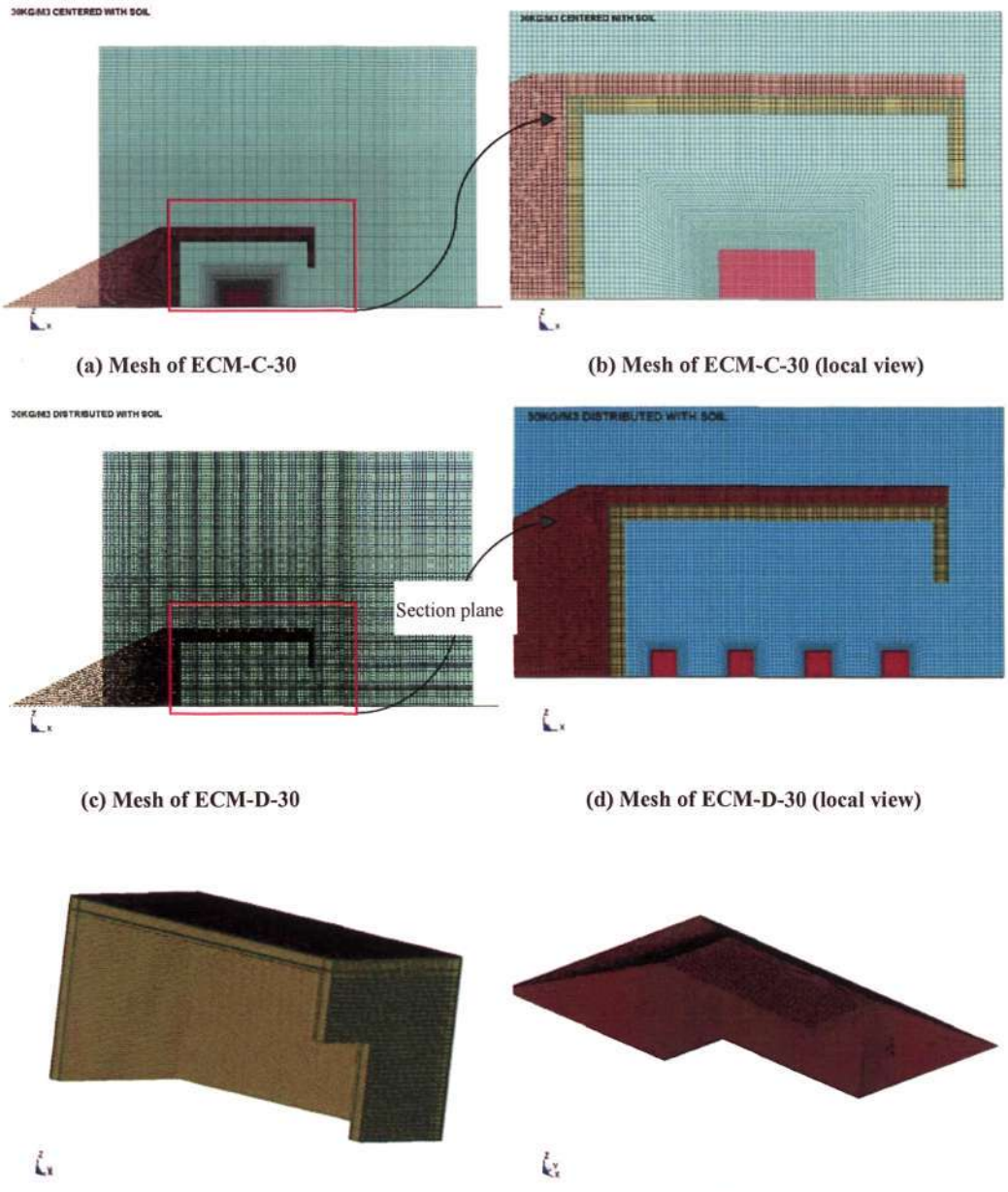

(a) Mesh of ECM-C-30

(b) Mesh of ECM-C-30 (local view)

(c) Mesh of ECM-D-30

(d) Mesh of ECM-D-30 (local view)

(e) Mesh of reinforced concrete box

(f) Mesh of soil cover

Fig. 6.2 Overview of the model mesh

Table 6.1 Details about the Eulerian part

Cases	Dimension(m^3)		Number of Element		Element Size (mm^3)	
	Air	TNT	Air	TNT	Air	TNT
AGM-C-30	38×20×20	2.64×1.32×1.32	3,407,300	16,000	140^3 ($5.7mm/kg^{1/3}$)	66^3 ($2.7mm/kg^{1/3}$)
ECM-C-30	29.2×11.2×20	2.64×1.32×1.32	1,909,700			
AGM-D-30	38×20×20	8×0.831^3	3,661,233	15,680	125^3	59×59×83
ECM-D-30	29.25×11.25×20	8×0.831^3	2,106,108			
AGM-C-2.5	23×10×10	1.153×0.5765×0.5765	2,017,490	16,000	100^3 ($9.3mm/kg^{1/3}$)	28.8^3 ($2.7mm/kg^{1/3}$)
ECM-C-2.5	23×10×10	1.153×0.5765×0.5765				
AGM-D-2.5	23×10×10	8×0.3632^3	1,976,250	18,000	100^3	26×26×36
ECM-D-2.5	23×10×10	8×0.3632^3				

6.2.4 Materials model

The empirical Jones-Wilkins-Lee (JWL) equation of state is used in the simulation of the ignition and growth of products of the explosive reaction. The air is modeled to represent the medium in which the blast wave propagates. A linear polynomial equation of state is used to simulate the air behavior (Lu, Gong et al. 2005).

In the present study, the "pseudo-tensor concrete" (LS-DYNA 2007) is employed to model the reinforced concrete structure. This model has been used to analyze buried steel reinforced concrete structures subjected to impulsive loadings.

The effect of reinforcement on the reinforced concrete behavior is simulated by a mixture material model. In this mixture model, a reinforcement fraction f_r, is defined along with properties of the reinforcement material. The bulk modulus, shear modulus, and yield strength are then calculated from the mixture rule, e.g., for the bulk modulus the rule gives

$$K = (1 - f_r)K_c + f_r K_r, \tag{6.1}$$

where K_c and K_r are the bulk modulus for the concrete and the reinforced steel, respectively. The modulus is updated as damage in the concrete (and steel) is accumulated. The relative importance of concrete in the mixture decreases as damage increases. The mixture model gives an isotropic effect in the material instead of the true anisotropic material behavior.

In this thesis, a reasonable approach would be adopted: use the mixture elements only where the reinforcing exists and plain elements elsewhere. Mixture elements with 500 MPa reinforced steel fraction 0.156 and 0.321 (indicated as Mix156 element and Mix321 element) are employed in simulation.

The earth cover is simulated by material 147 (*MAT_147_N) (Lewis 2004; Reid, Coon et al. 2004) in LS-DYNA. The default properties determined for soils used at the University of Nebraska (Lincoln) is adopted (LS-DYNA 2007). This is an isotropic material with damage and is available for solid elements. The model has a

modified Mohr-Coulomb surface to determine the pressure dependent peak shear strength. It was developed for applications involving road base soils.

6.3 Results of break-up and deformation

6.3.1 Break-up pattern under high loading density 30 kg/m^3

The break-up pattern of all 4 cases under high loading density are presented and compared. Fig. 6.3 shows the overall deformation and breakup of the 4 cases under 30 kg/m^3 at 6 time points. They are 5, 10, 15, 20, 25 and 30ms.

AGM-C-30 ECM-C-30

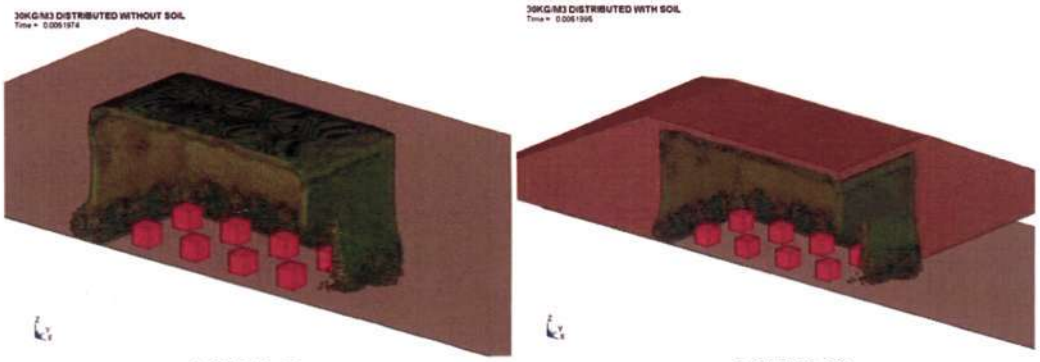

AGM-D-30 ECM-D-30

(a) 5ms

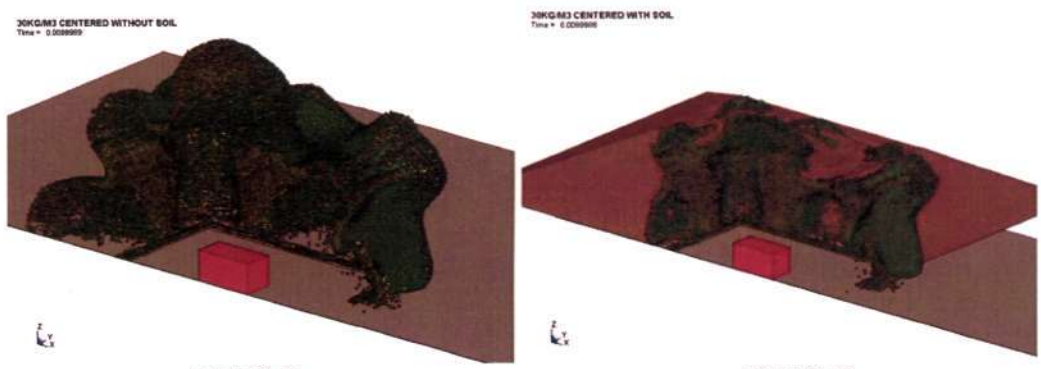

AGM-C-30 ECM-C-30

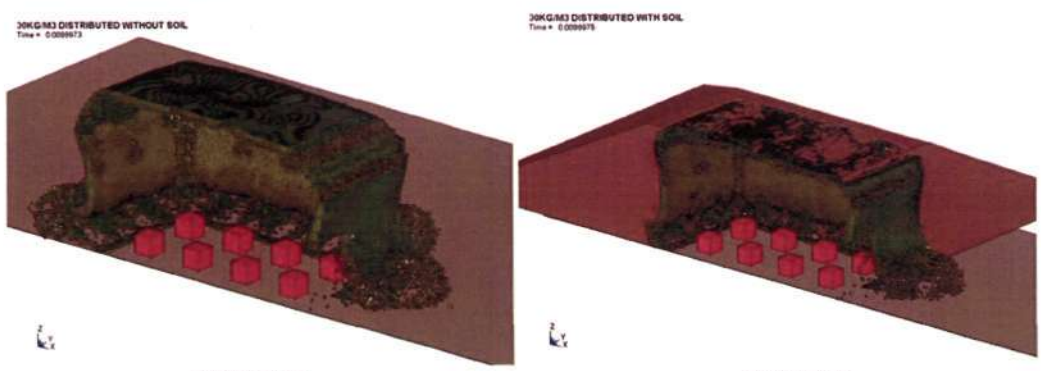

AGM-D-30 ECM-D-30

(b) 10ms

AGM-C-30

ECM-C-30

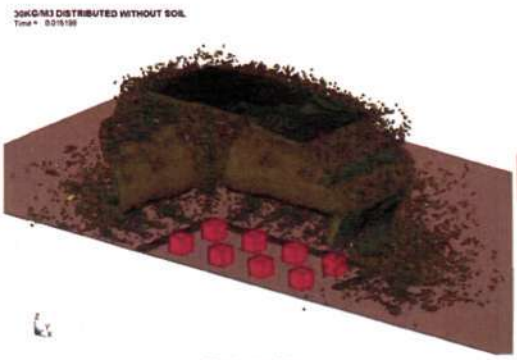

AGM-D-30

ECM-D-30

(c) 15ms

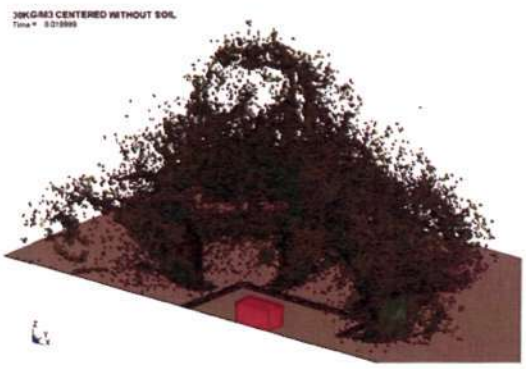

AGM-C-30

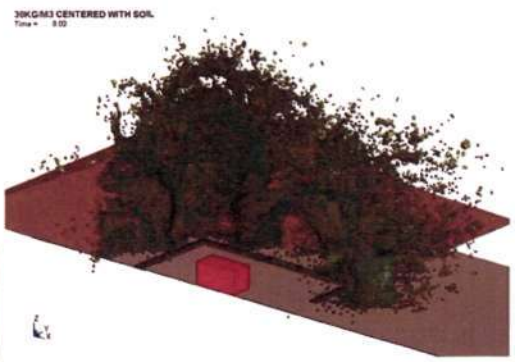

ECM-C-30

AGM-D-30

ECM-D-30

(d) 20ms

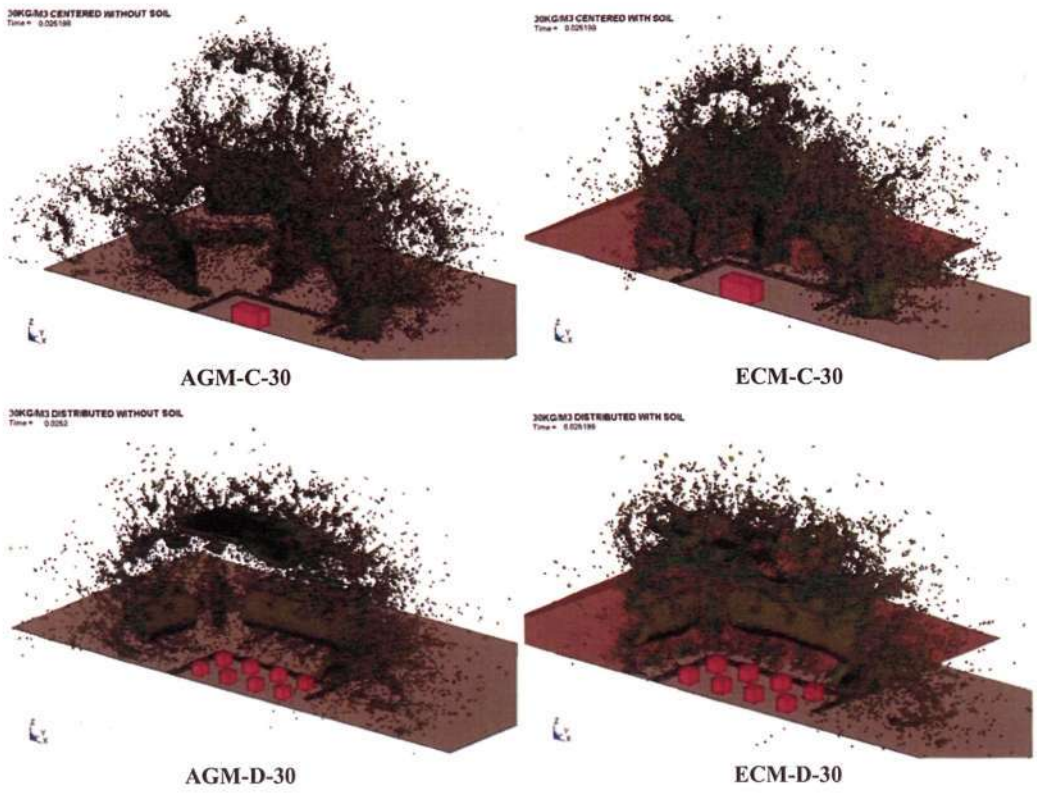

(e) 25ms

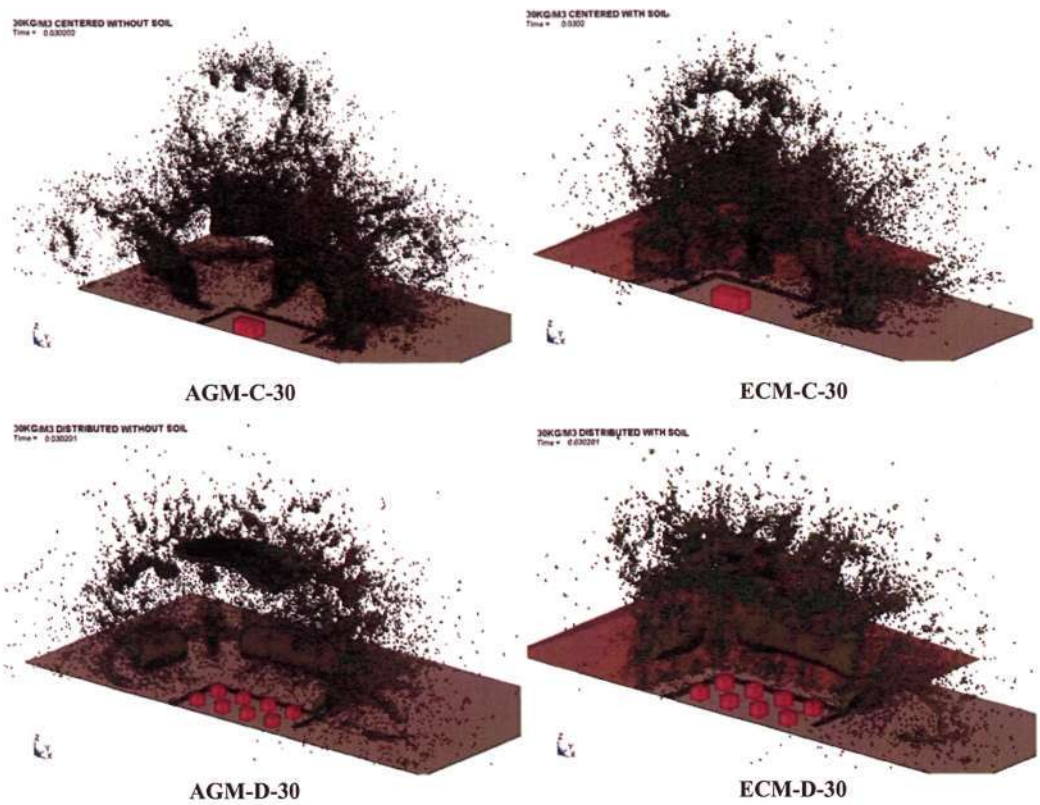

(f) 30ms

Fig. 6.3 Break-up pattern comparison under high loading density 30 kg/m^3

At 5ms, AGM-C-30 is the most seriously damaged among the 4 cases. The roof center and the lower part of the two walls without door are the first two locations of deformation and breakup, which are in agreement of shock wave propagating with a spherical shape. AGM-D-30 generates serious break-up at the lower part and obvious damage at some places due to the composite shock-wave effect. Part of soil cover of ECM-C-30 gets eroded at top center. The soil cover in ECM-D-30 maintains well.

While at 30ms, all structures have broken up totally. The corner and the connection location start to break up because of the reflection and constrain of overpressure. The roof of AGM-D-30 still remains integrity to some extent though the structure has broken up. While the roof of ECM-D-30 turns into several big fragments because of the soil effect and the composite shock wave effect on structure.

For ECM, the soil prevents most of the debris, which is formed from the two walls without door, from free flying. However, the roof debris is free as the soil elements above the roof have eroded away. At high loading density 30 kg/m^3, the soil cover has little effect on the structural intactness .

The conclusions drawn from the observations from break-up patterns are:

1) In all cases of high loading density of 30 kg/m^3, all the RC structure break up into debris. Under this high density loading, the soil cover has little effect on the structural integrity.

2) ECM case has lower velocity than AGM case, and the distributed case has lower velocity than the centered case. Under this high density loading, the soil cover has certain effect on decreasing the roof debris velocity.

3) For ECM, the soil prevents most of the debris, which is formed from the two walls without door, from free flying. However, the roof debris is free as the soil elements above the roof have eroded away.

6.3.2 Deformation pattern under low loading density 2.5 kg/m^3

For the low loading density, only the deformation and cracks are captured. The whole structure remains integrity in all the 4 case. The deformation pattern under low loading density 2.5 kg/m^3 are presented and compared.

Table 6.2 shows the deformation and fracture of the 4 cases under 2.5 kg/m^3 at the computational cut-off time, 27ms for centered TNT stack cases and 30ms for distributed TNT stack cases. The 2nd row of Table 6.2 shows the overall deformation at the cut-off time while 3rd-8th rows show the fracture patterns at 6 chosen different regions.

Table 6.2 Deformation pattern comparison under low loading density 2.5 kg/m^3

AGM-C-2.5	ECM-C-2.5	AGM-D-2.5	ECM-D-2.5

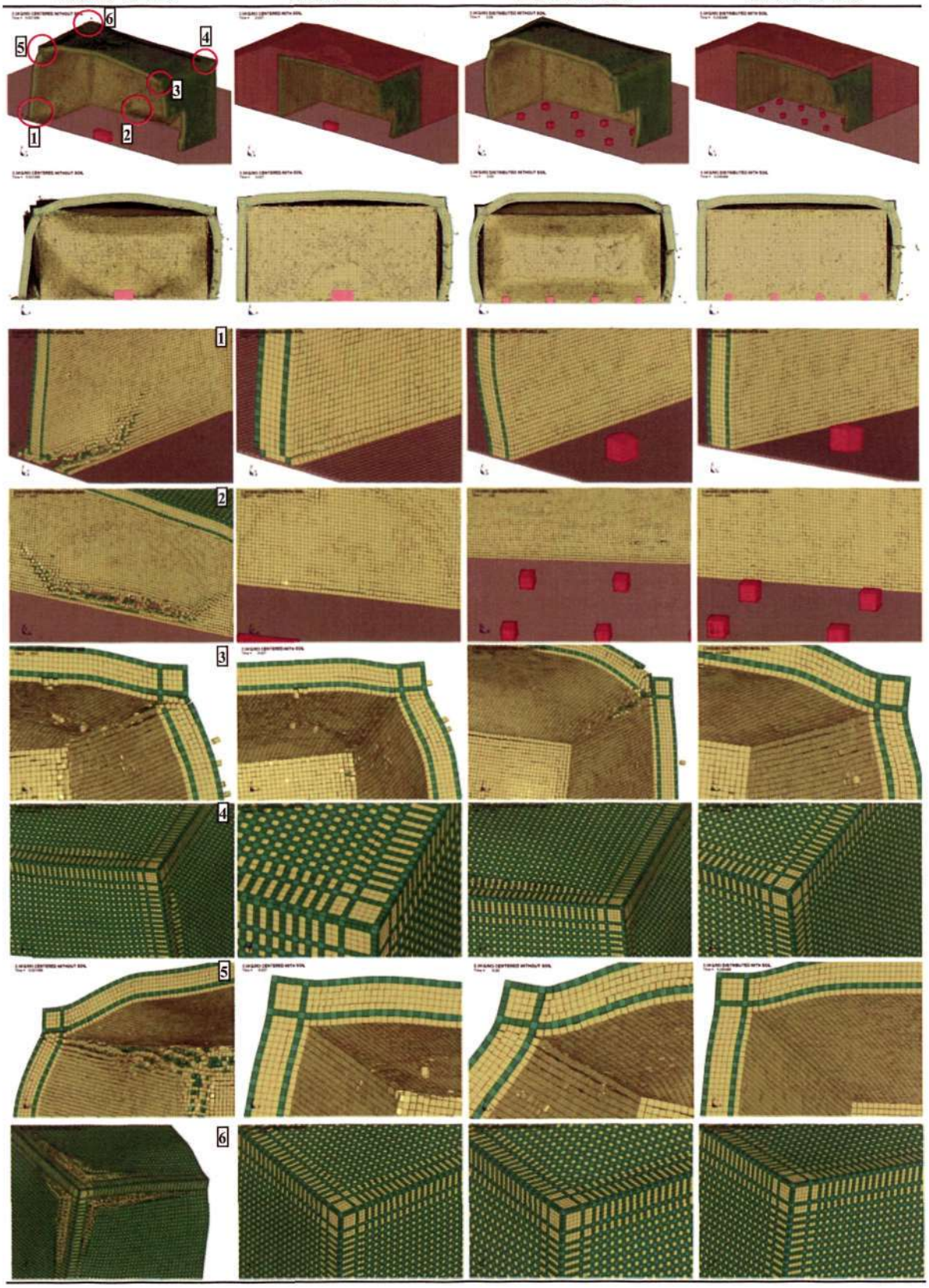

The magazine structures remain integral with deformation and cracks. The soil cover maintains in place in ECM cases. In AGM-C-2.5, obvious wide cracks are detected at all regions except for region 4 with only several trivial cracks. While in ECM-C-2.5, only the trivial cracks are investigated. In AGM-D-2.5, the cracks are easily seen in region 3 and 5 only, where the trivial cracks are captured in ECM-D-2.5.

These phenomena indicate that under low loading density of 2.5 kg/m^3, the soil cover has considerable effect on the structural deformation and fracture, while under the high loading density the soil cover has little effect.

If the TNT stack formats (centered and distributed) are concerned, more serious and obvious cracks have been found in the centered TNT cases. Because the distributed stack format probably ease up the detonation effects.

The conclusions drawn from the observations from deformation and cracking patterns are:

1) The soil cover is inclined to protect the structure for minor deformation and cracks are investigated in ECM cases.

2) Distributed TNT stack format probably eases up the detonation effects under low loading density.

6.4 Results of debris throw

6.4.1 Cases

Debris throw cases are developed from those in break-up and deformation simulation. ECM-C-30 and ECM-D-30 are considered for the soil blocking effect. There are results of 9 cases in all. The basic information of the cases is listed in Table 6.3 below.

Table 6.3 Debris free flying cases information

Case No.	Name	Charge Density	Charge Distribution	Cover With Soil	Note
1	AGM-C-30	30 Kg/m^3	Centered	No	
2	ECM-C-30	30 Kg/m^3	Centered	Yes	
3	AGM-D-30	30 Kg/m^3	Distributed	No	
4	ECM-D-30	30 Kg/m^3	Distributed	Yes	
5	ECM-C-30-SB	30 Kg/m^3	Centered	Yes	With soil blocking effect^
6	ECM-D-30-SB	30 Kg/m^3	Distributed	Yes	With soil blocking effect^
7	AGM-C-2.5	2.5 Kg/m^3	Centered	No	
8	ECM-C-2.5	2.5 Kg/m^3	Centered	Yes	
9	AGM-D-2.5	2.5 Kg/m^3	Distributed	No	

^Note: Soil blocking effect

In the LS-DYNA simulation process of breaking up, the traveling path of broken-up concrete fragments are unblocked by the covered soil even if the soil element does not erode away. As such, the resulting ejecting velocities of those fragments will be over-estimated. The LS-DYNA simulation stops at about 30 ms (t_e) after detonation. At that time, the blast overpressure drops to zero, and those un-eroded covered soil will remain un-eroded and travel at a speed slower than some ejected fragments behind them. If the blocking effect is neglected, those fragments will fly further. To correct this, the height h_e of the un-eroded soil at time t_e is registered, and all fragments located at positions lower than h_e will be assigned a nominal velocity of much reduced value. As the front wall of magazine has no covered soil, the velocity of fragments formed from there will not be reduced. Cases 2 and 4 are re-investigated by considering this blocking effect. Results are presented in Cases 5 and 6, respectively.

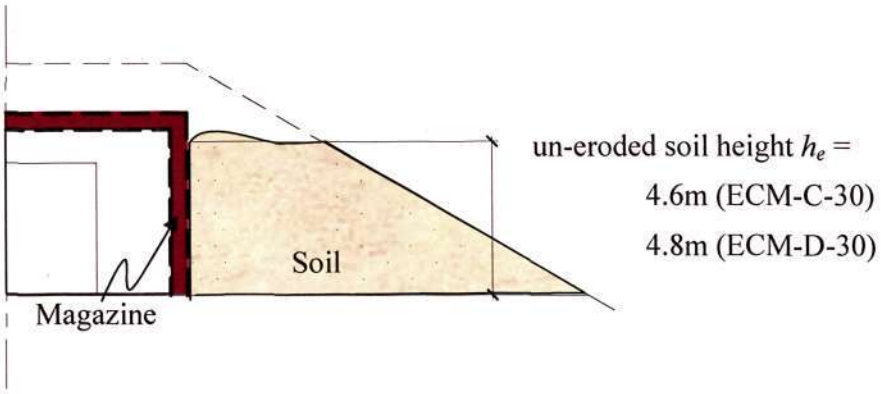

Fig. 6.4 Soil blocking effect

6.4.2 Debris number

Using the same definition and presentation format in the Kasun Test (Berglund, Carlberg et al. 2006), debris numbers for each case are sorted into Mass Bins as shown in Table 6.4.

Table 6.4 Mass Bins and Debris numbers

Mass Bin		1	2	3	4	5	6	7	8	
Debris	M^{min}	24.495	9.753	4.31	1.815	0.772	0.273	0.137	0.055	
mass	M^{max}		24.494	9.752	4.309	1.814	0.771	0.272	0.136	
(kg)	$M^{ave.}$	34.2	14.3	6.08	2.54	1.08	0.454	0.191	0.082	
		Debris Number								Sum.
High Density	AGM-C-30	118	60	184	726	147697	0	0	0	148785
	ECM-C-30	58	100	348	1133	142417	0	0	0	144056
	AGM-D-30	171	132	1687	2757	143978	0	0	0	148725
	ECM-D-30	2221	360	1849	1818	140184	0	0	0	144432
	ECM-C-30-SB	2	2	199	639	79363	0	0	0	80205
	ECM-D-30-SB	17	9	810	929	88096	0	0	0	89861
Low Density	AGM-C-2.5	0	4	658	1609	8194	0	0	0	10465
	ECM-C-2.5	0	0	4	273	1053	0	0	0	1330
	AGM-D-2.5	0	0	4355	911	2520	0	0	0	7786

Observations from the table are as follow.

1. There are no debris falling into Mass Bins 6, 7 and 8, but the numbers in Mass Bin 5 are huge. Note that Mass Bin 5 is actually collection of all masses less than 0.772 kg because this is the smallest unbreakable element mass that can be afforded in the present *LS-DYNA* simulation process due to the limit of computer capacility. Information on further breakdowns into Bins 6~8 could be obtained if smaller element size were employed.

2. In high-density load cases, more fragments are created and thus the debris numbers are significantly higher than those in low-density load cases.

3. In all 4 high-density load cases (without implantation of soil-blocking effect), the total number of debris are almost the same. So are the 2 cases with soil-blocking effect. It indicates that the soil cover and loading format ('center' or 'distributed') only result in different distributions of fragment sizes under high-density load.

4. In high-density load cases, the soil blocking-effect could reduce the debris numbers by 40%. It is because the velocity of the blocked debris is apparently reduced to zero, and thus all of them do not reach any Bin.

5. In the low-density load cases, the total number of debris decreases but it results in more bigger-size debris if the load format is changed from 'center' to 'distributed'. In addition, the total number of debris will drop markedly if the magazine is earth-covered.

In a nutshell, the load density causes the most significant difference in debris number. The soil cover could also significantly reduce the total number of debris in both high-density and low-density load cases. The 'distributed' load format will result in more bigger-size debris than those from the 'center' load format.

6.4.3 Debris ejection velocity distribution

Fig. 6.5 and Fig. 6.6 show the debris ejection velocity distributions for 4 high-density load cases.

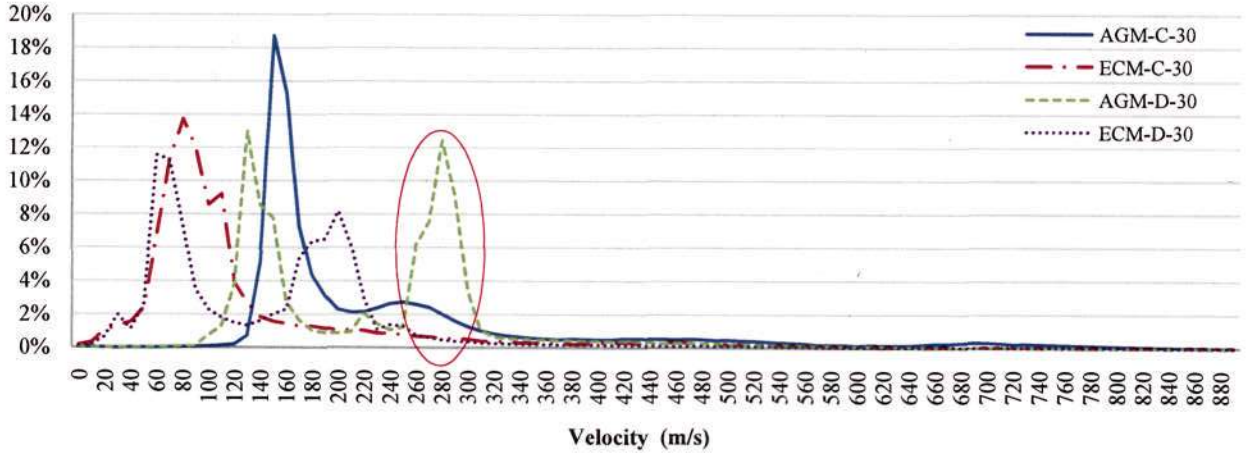

Fig. 6.5 Debris ejection velocity distribution (at 10m/s interval)

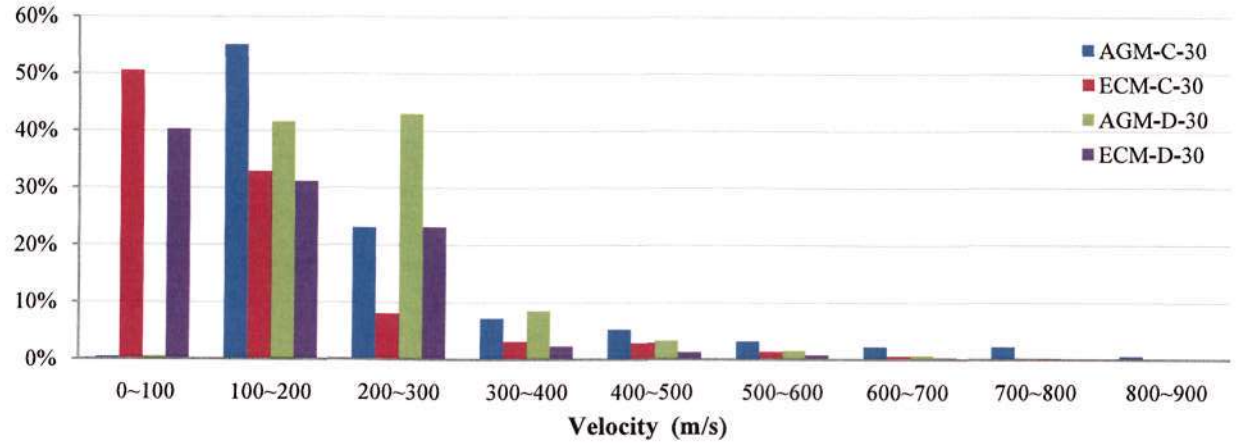

Fig. 6.6 Debris ejection velocity distribution (at 100m/s interval)

Seen from Fig 6.5 and Fig. 6.6, the two centered-charge cases have one distribution peak, while the distributed-charge cases have two peaks. The two cases without covering soil have higher average velocity, as higher percentage-distributions occurs at higher velocities. The two cases with covering soil have a relatively high percentage-distribution in the lowest velocity interval [0, 100m/s], in contrast to 'uncovered' cases where few debris falls in that low-speed interval.

It should note that peak percentage-distribution occurs at high velocity interval does not necessarily lead to the most dangerous hazard. For example, one of the peak percentage-distribution for the Case AGM-D-30 occurs in the high velocity interval [250m/s, 300m/s] (as circled in Fig. 6.5). The debris size may be small though the quantity may be large; or the ejection angle may be close to 90 degree such that the debris does not fly far away.

Another way of measuring the hazard may be the velocity range, which can be obtained from a cut-off % of accumulated debris number. Table 6.5 shows the accumulated distribution of debris number for the 4 high-density load cases (AGM-C-30, ECM-C-30, AGM-D-30 and ECM-C-30). If the cut-off level is set at 95%, the debris velocity range will be derived (by interpolation) from Table 6.6. The velocity ranges are shown in Table 6.5.

Table 6.5 Debris ejection number distribution (accumulated)

Velocity Range (m/s)	Debris Number Percentage			
	AGM-C-30	ECM-C-30	AGM-D-30	ECM-D-30
0~100	0.5%	50.6%	0.5%	40.3%
0~200	55.6%	83.4%	42.2%	71.5%
0~300	78.8%	91.5%	85.2%	**94.8%**
0~400	86.0%	**94.6%**	**93.8%**	97.1%
0~500	91.4%	97.6%	97.1%	98.4%
0~600	**94.6%**	99.0%	98.8%	99.3%
0~700	96.9%	99.6%	99.5%	99.7%
0~800	99.2%	99.9%	99.8%	99.9%
0~900	99.8%	100.0%	100.0%	100.0%
0~1000	100.0%	100.0%	100.0%	100.0%

Table 6.6 Debris ejection velocity range at 95% accumulated level

Cases	AGM-C-30	ECM-C-30	AGM-D-30	ECM-D-30
Vel. range (m/s)	0 ~ 650	0 ~ 410	0 ~ 430	0 ~ 300

Fig. 6.7 demonstrates the soil-blocking effect on debris velocity distribution. The 2 cases of high-density centered-charge and distributed-charge are considered. It can be seen that the most significant difference is detected at the lowest velocity interval [0,100m/s]. It indicates that most of the debris blocked by soil fall within the low velocity range lesser than 100 m/s.

In a nutshell, the centered-charge case without soil cover yields higher debris ejection velocity range; while the distributed-charge case with soil cover yields the lower debris ejection velocity. Moreover, the soil-blocking effect is more prominent to those low-velocity debris.

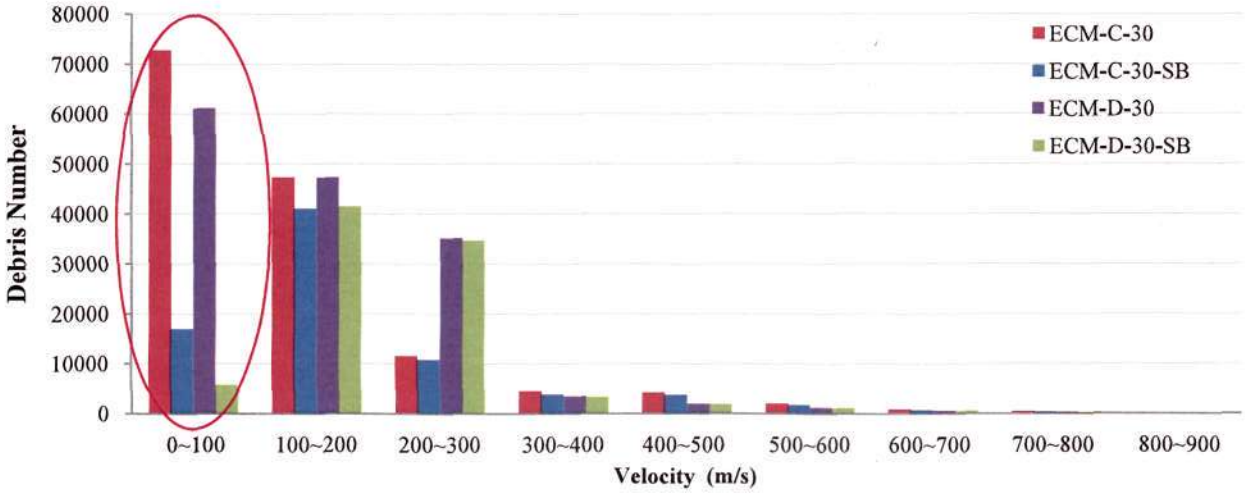

Fig. 6.7 Debris ejection velocity distribution (soil blocking effect)

6.4.4 Debris distribution in directions

Debris numbers settled on ground are counted in 19 equal sectors, namely Sector A to Sector S over a 190-degree view. The angle of each sector is 10 degrees, with the first one starting from -5° and the last one ending at 185°.Fig. 6.8 depicts of the collecting sectors.

The debris spatial distribution for the 4 high-density load cases is shown in Fig 6.9. It can be seen that 25% of debris fall into sector J, which is normal to the magazine side wall, except in the Case ECM-C-30, where the 25% equally splits into the two neighboring sectors I and J.

For the distributed-charge cases, secondary peak percentage-distributions are seen in sectors A and S, which are normal to the magazine front wall and rear wall; while for the centered-charge cases, secondary peak %-distributions are seen only in sector S.

Apparently, the further away from the directions normal to the magazine walls (front, side and rear), the fewer debris number will be.

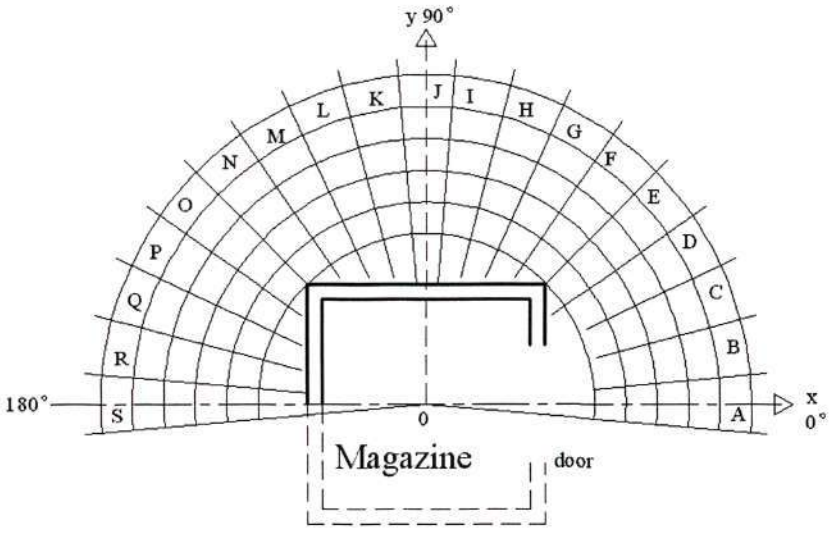

Fig. 6.8 Diagram of debris collecting sectors

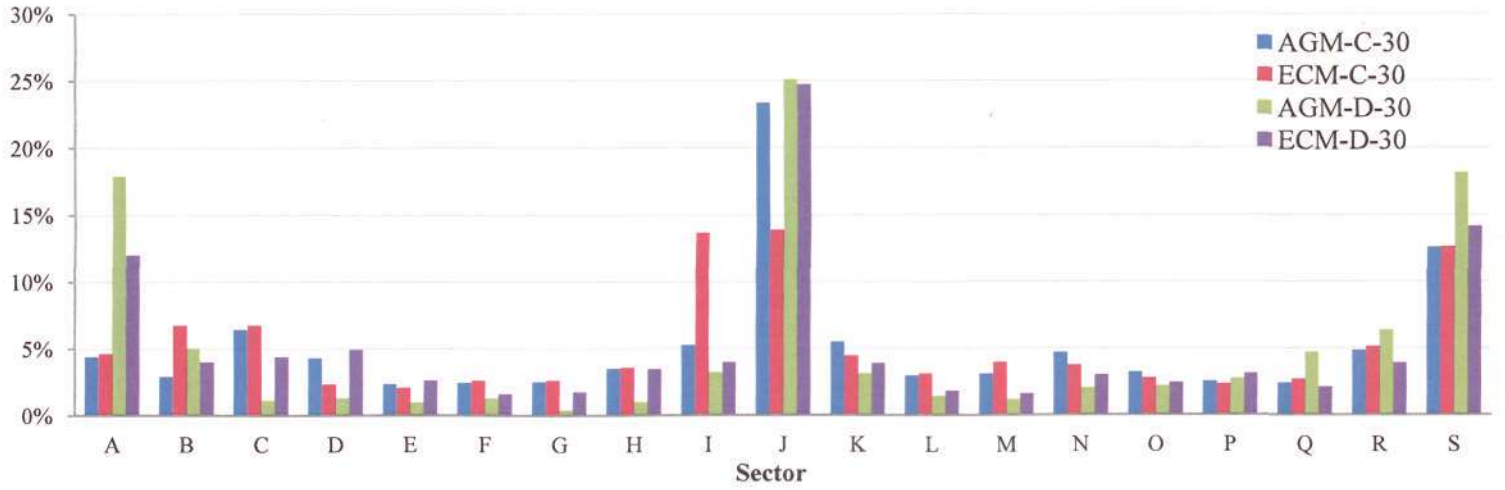

Fig. 6.9 Debris distribution in sectors

6.4.5 Debris distribution at distances

Another way to view the debris distribution is to count the debris in radial direction measured away from the magazine. Debris number settled on ground is counted at every 10m (radial) intervals of the 190°-wide sector.

Fig. 6.10 shows the debris distributions for the 4 high-density load cases, obtained by using a lower value of drag coefficient C_d = 1.2. When higher values of drag coefficients (C_d = 1.6 or 2.0) are used, almost the same distribution pattern is obtained, except that the throw distances are reduced proportionally for higher value of C_d. It is also noted that most of the debris falls within the nearest 100m. The percentages of debris within the 100m are shown in Table 6.7

Observed from Fig. 6.10, that it is obviously that 35% to 60% of the debris is within 100m.

Table 6.7 Percentage of debris within 100m

Cases	AGM-C-30	ECM-C-30	AGM-D-30	ECM-D-30
Debris within 100m	34.5%	57.5%	38.8%	47.2%

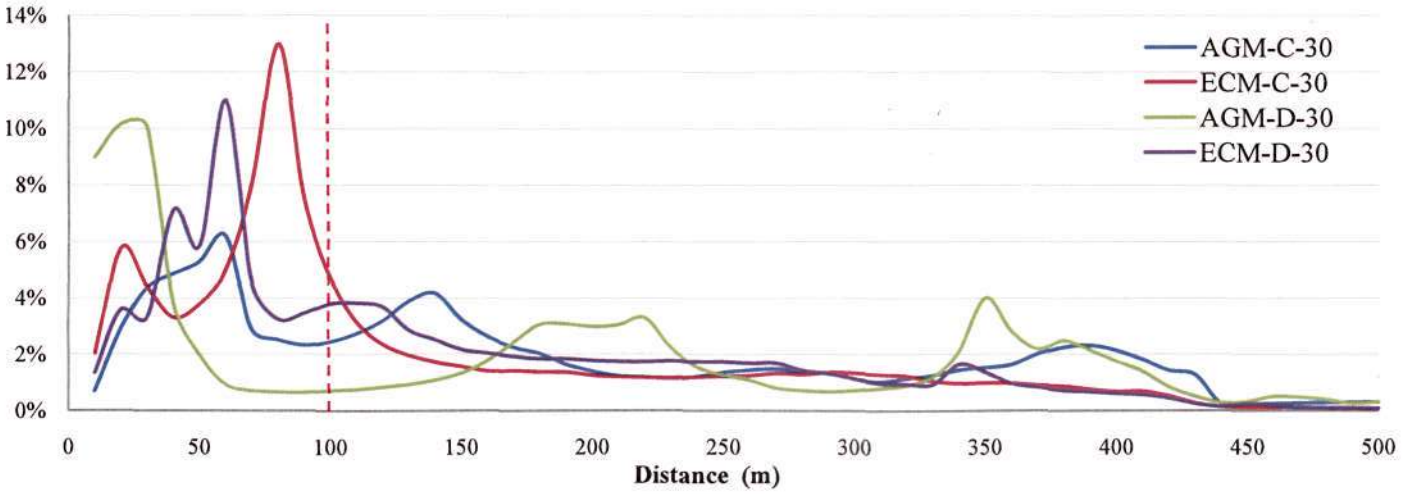

Fig. 6.10 Debris distribution at different distances (C_d=1.2)

In this connection, one can device another way of measuring the hazard by associating it with the debris flying range, which can be obtained from a cut-off % of accumulated debris number. Table 6.8 shows the throw-distance ranges for the 6 high-density load cases (AGM-C-30, ECM-C-30, AGM-D-30, ECM-C-30, ECM-C-30-SB, and ECM-D-30-SB) for 3 different cut-off % (98%, 95% and 90%), obtained by using C_d = 1.2. The ranges of different values of C_d for Case ECM-D-30 are compared in Table 6.9.

Table 6.8 Debris flying ranges for different cut-off % (using Cd = 1.2)

Cases	AGM-C-30	ECM-C-30	AGM-D-30	ECM-D-30	ECM-C-30-SB	ECM-D-30-SB
	(m)	(m)	(m)	(m)	(m)	(m)
98%	480	410	480	410	420	330
95%	420	370	420	360	390	300
90%	400	320	390	320	350	270

Table 6.9 Debris flying ranges for different values of C_d (Case ECM-D-30)

Case ECM-D-30	C_d= 1.2		C_d= 1.6		C_d= 2.0	
	(1)	ratio	(2)	ratio	(3)	ratio
	(m)	(1) / (3)	(m)	(2) / (3)	(m)	(3) / (3)
98%	410	**1.58**	320	**1.23**	260	**1.00**
95%	360	**1.50**	280	**1.17**	240	**1.00**
90%	320	**1.52**	260	**1.24**	210	**1.00**

As seen from Table 6.8, soil cover could significantly reduce the debris flying ranges. The distributed-charge format would also result in significant reduction of the debris flying range, only if the soil-blocking effect is taken into account. On the other hand, Table 6.9 illustrates that the value of drag coefficient has significant influence on the resulting debris flying range. For the cut-off range of 90~98%, the

flying range obtained from using smaller C_d = 1.2 could be 1.5~1.6 times of that obtained from using a higher C_d = 2.0.

6.4.6 Debris scattering map

Debris scattering maps of the high-density load cases are presented in this section.

For each load case, the map is derived by using 3 different values of drag coefficient, that is, C_d = 1.2, C_d = 1.6 and C_d = 2.0. The scattering maps are presented in two forms. The first is plotted against the absolute debris number. The second is plotted against the normalized number (which is defined as debris number per m^2 in a cell). See Fig. 6.11 through Fig 6.18. The comparisons between cases with and without soil-blocking effect are presented last, in Fig. 6.19 through Fig. 6.20.

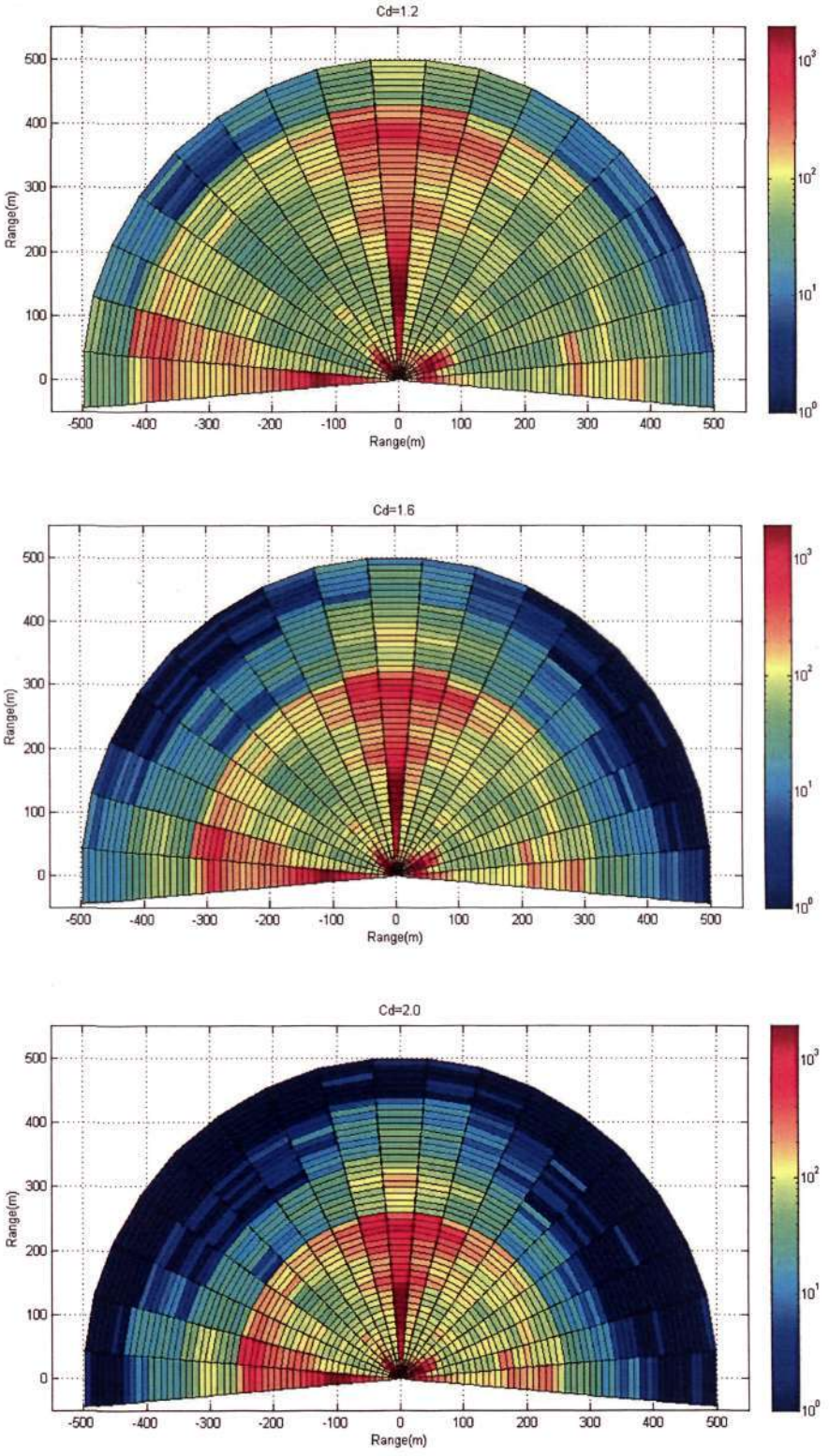

Fig. 6.11 Scattering map of case AGM-C-30

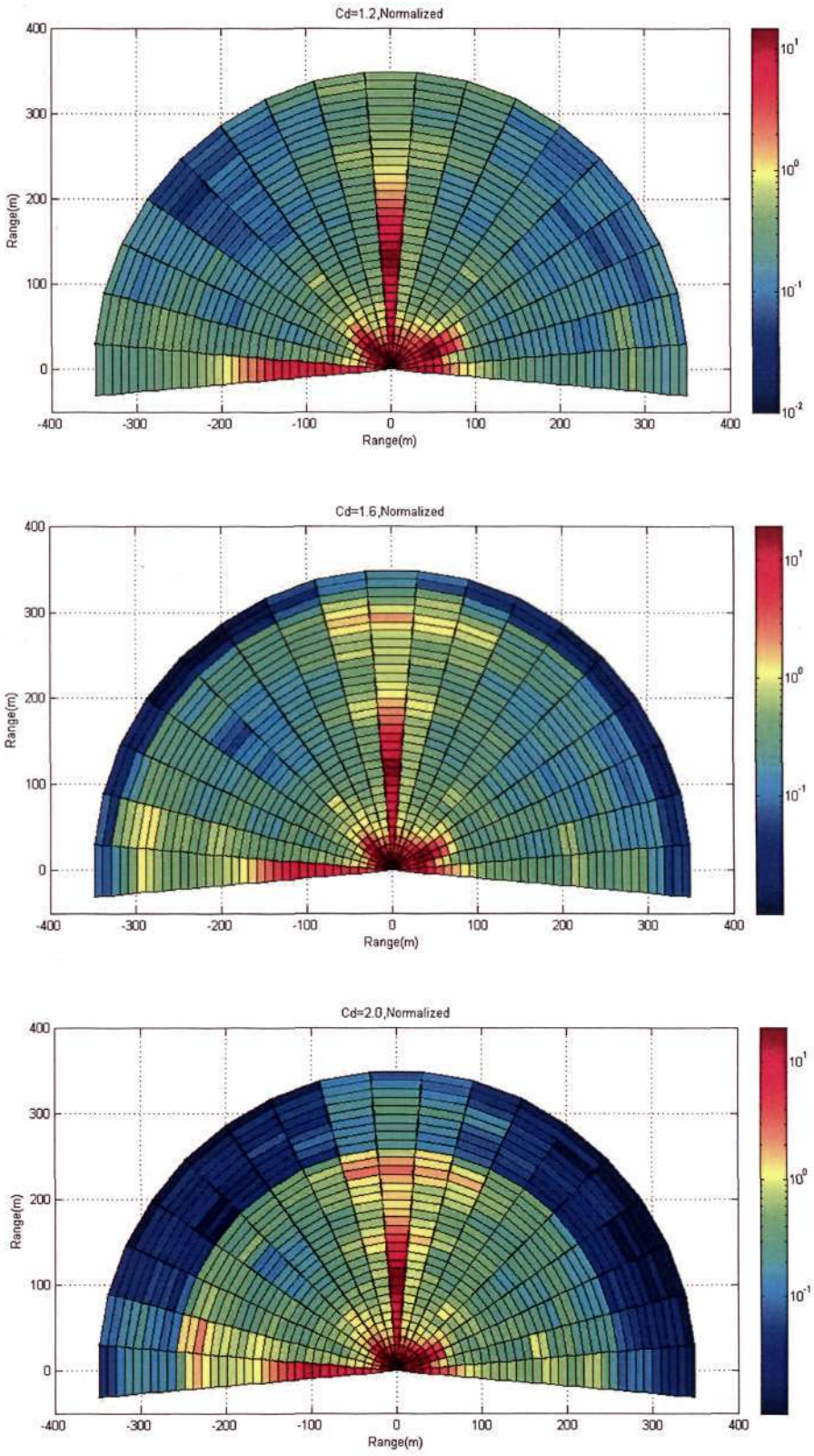

Fig. 6.12 Scattering map of case AGM-C-30 (Normalized)

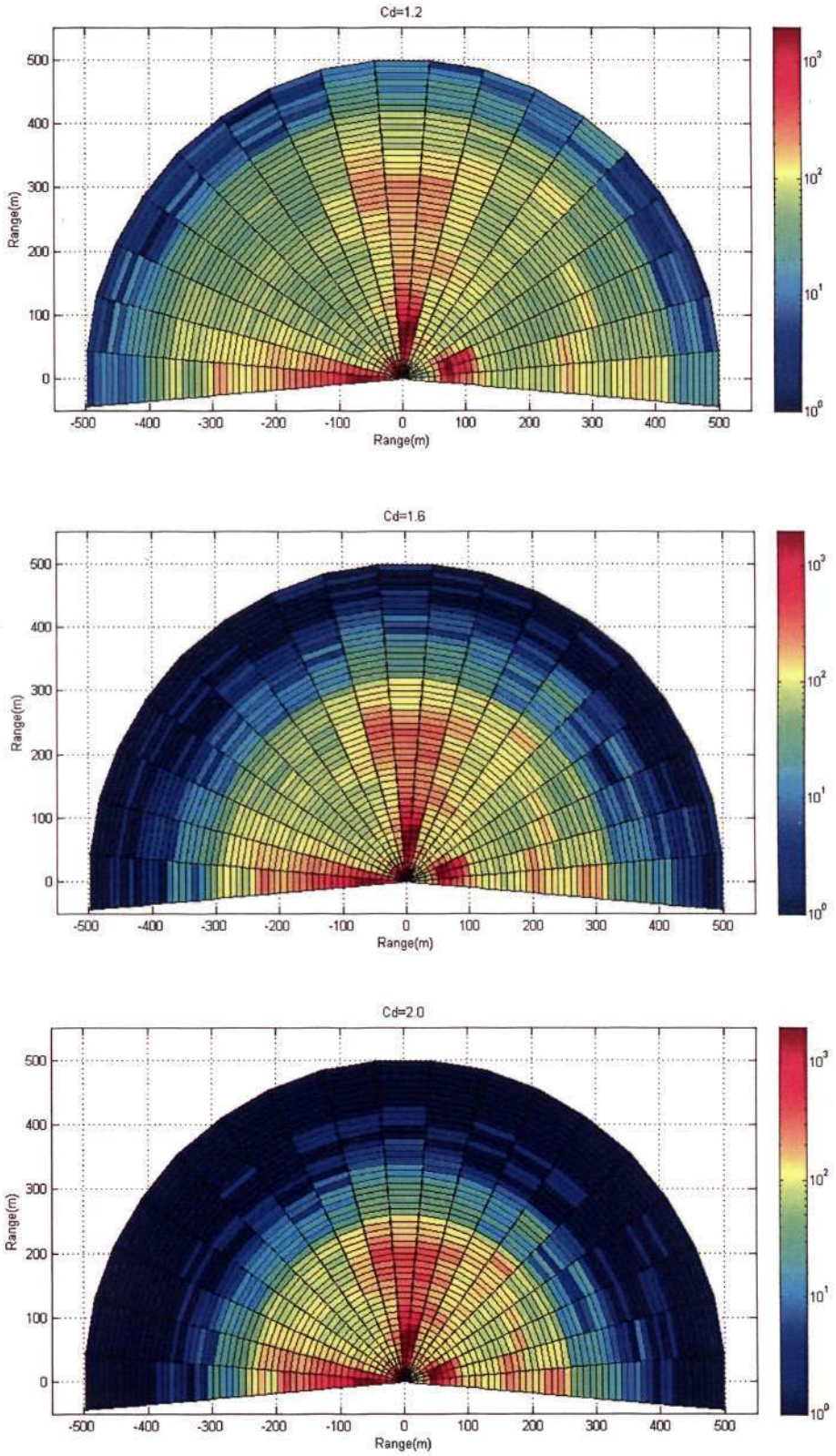

Fig. 6.13 Scattering map of case ECM-C-30

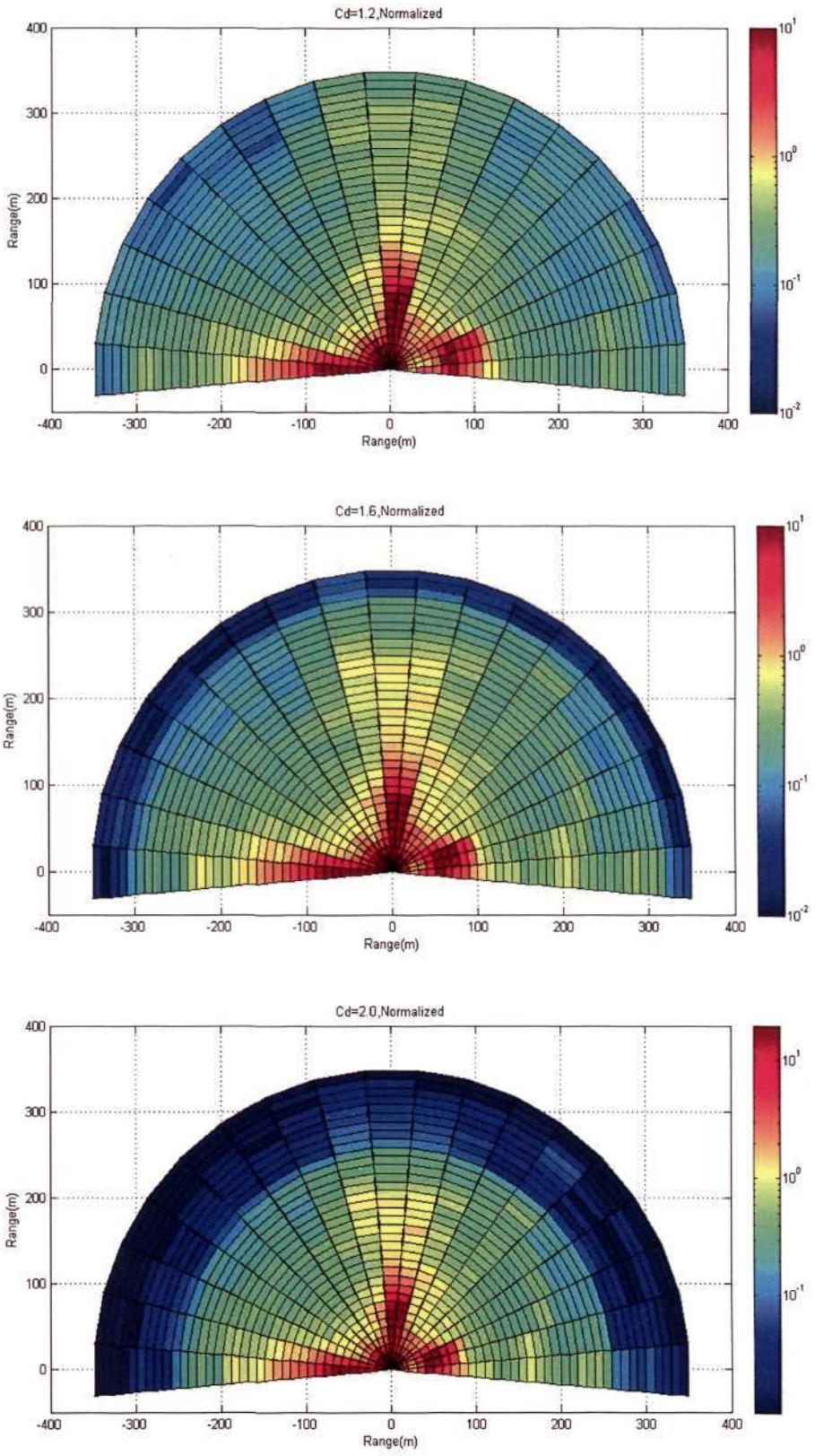

Fig. 6.14 Scattering map of case ECM-C-30 (Normalized)

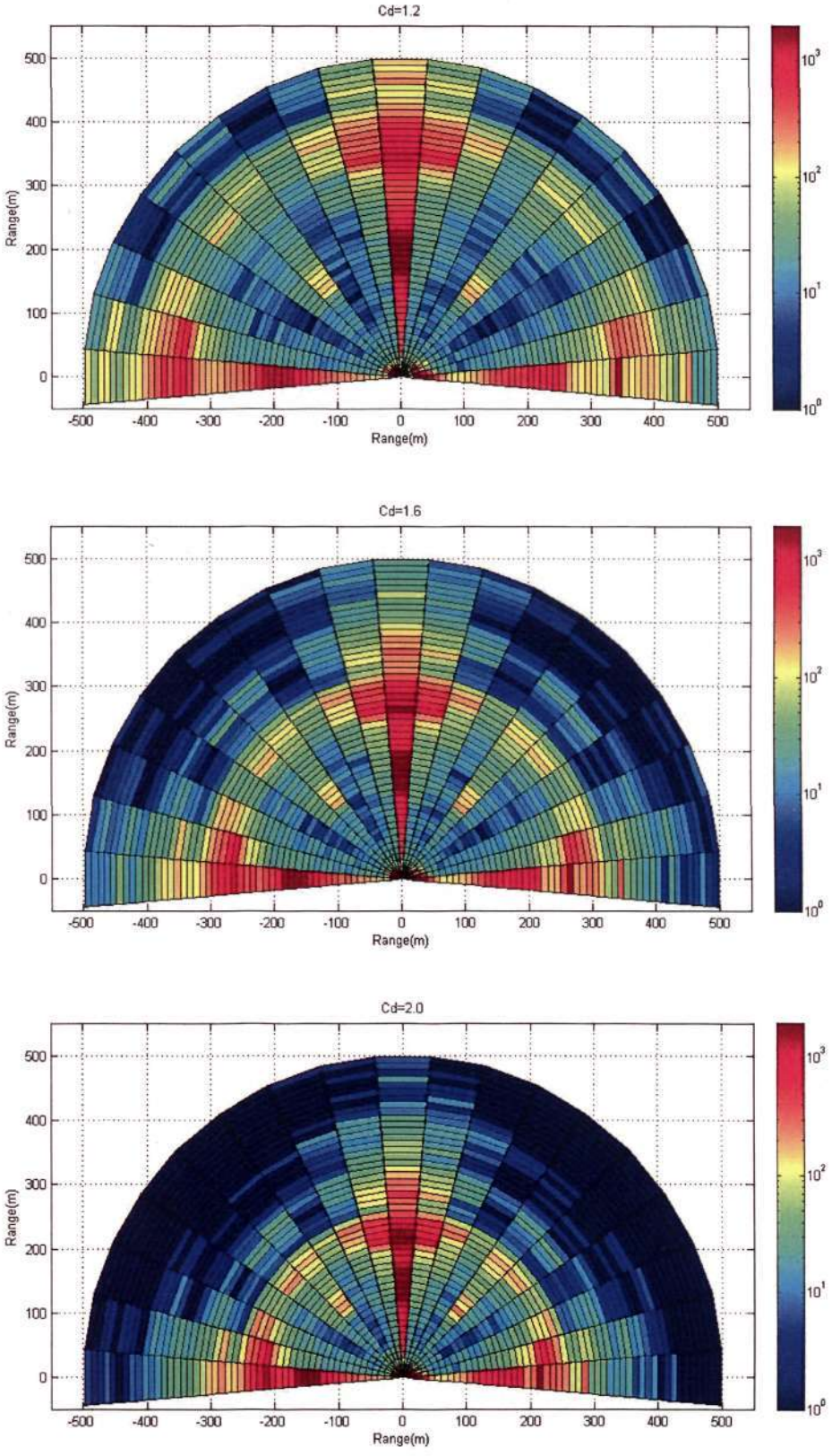

Fig. 6.15 Scattering map of case AGM-D-30

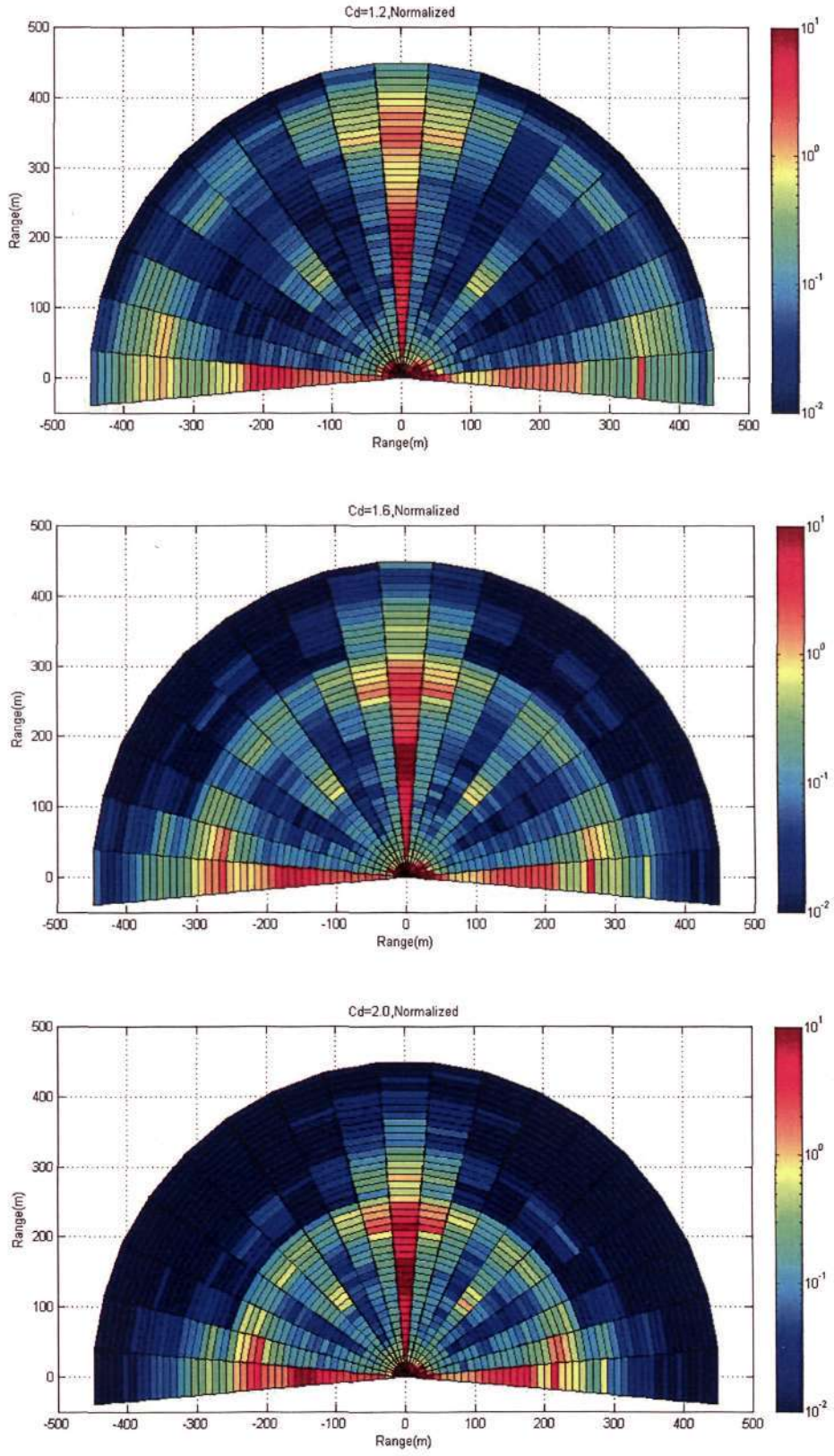

Fig. 6.16 Scattering map of case AGM-D-30 (Normalized)

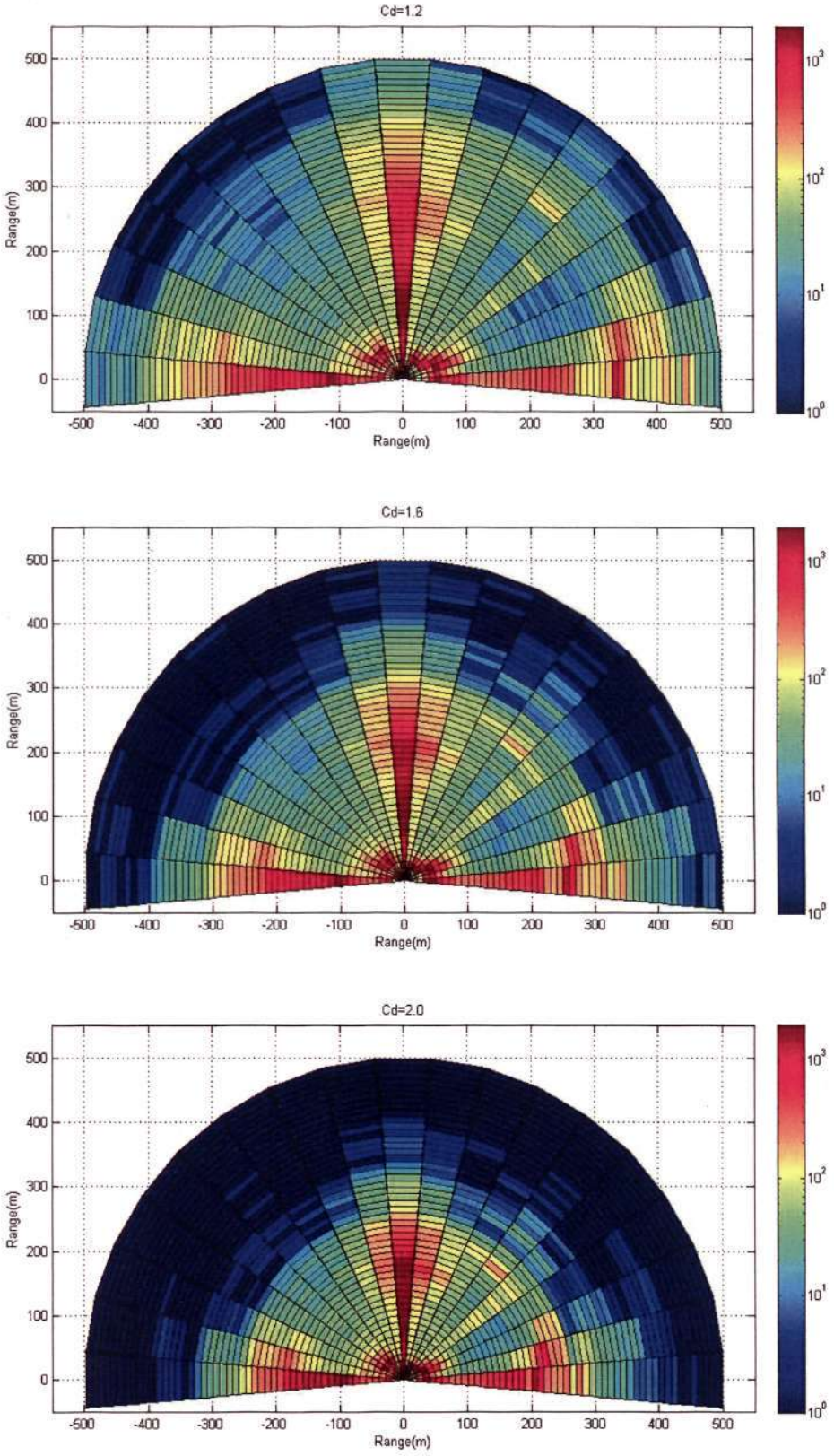

Fig. 6.17 Scattering map of case ECM-D-30

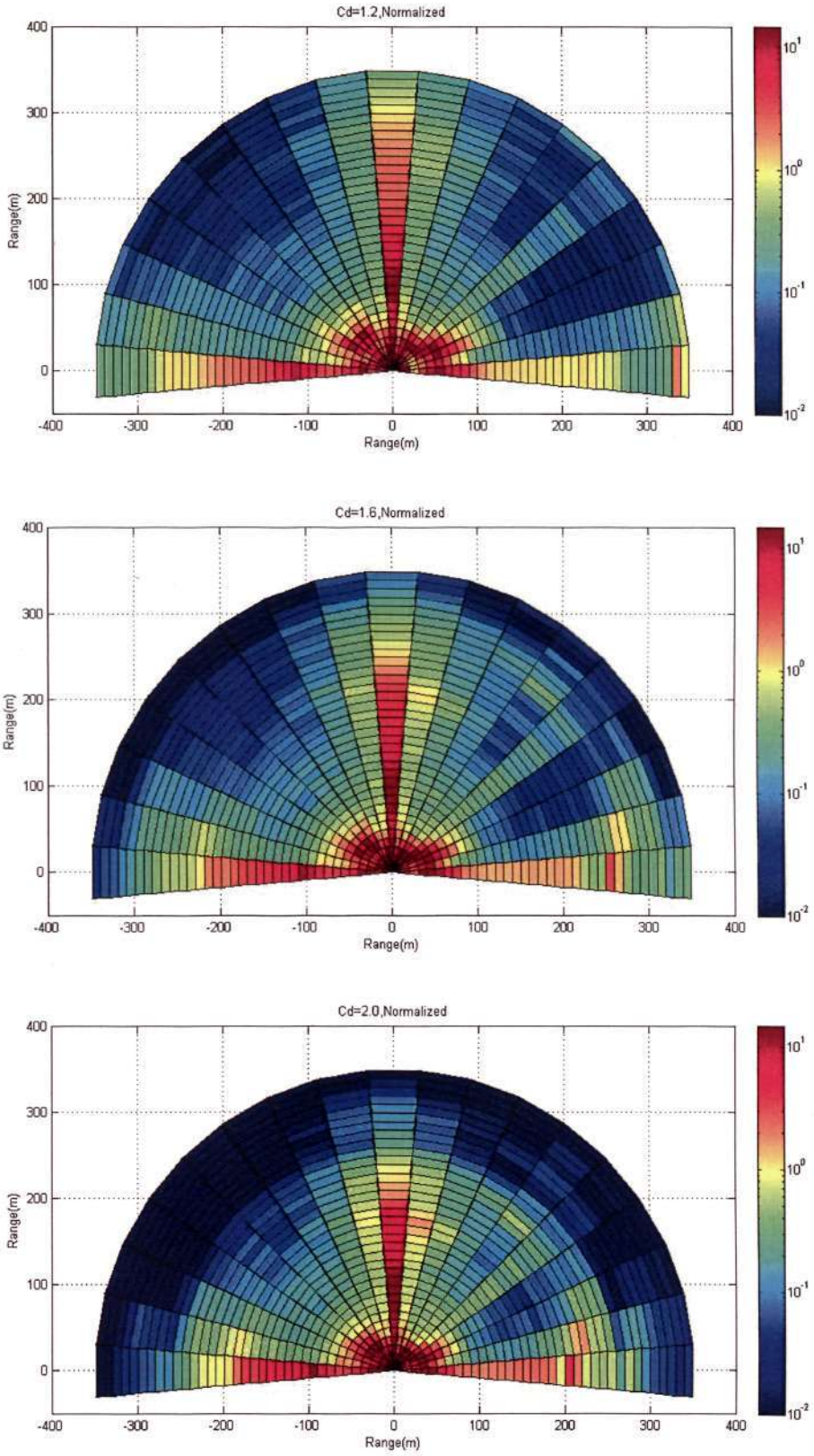

Fig. 6.18 Scattering map of case ECM-D-30 (Normalized)

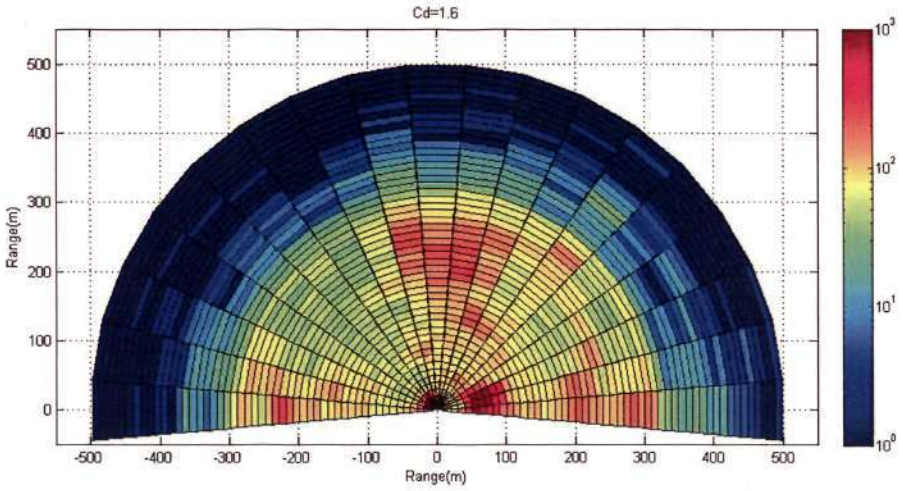

(a) Scattering map ofcase ECM-C-30-SB

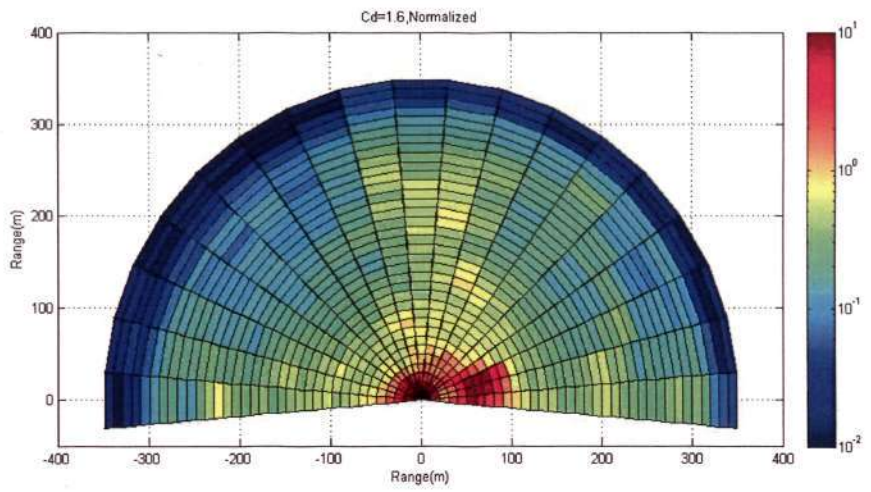

(b) Scattering map of case ECM-C-30-SB (Normalized)

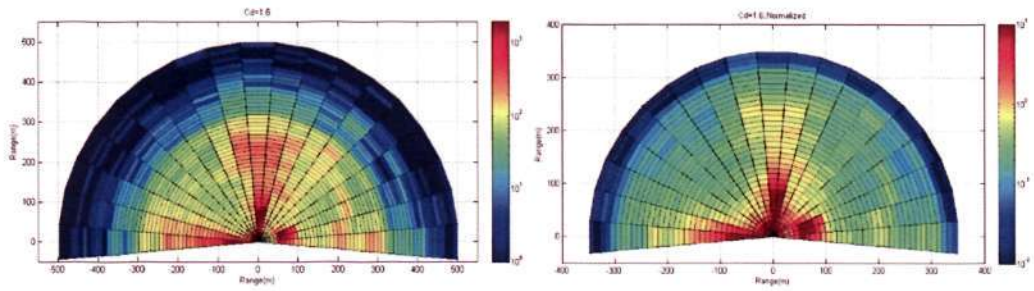

(c) Scattering map of case ECM-C-30 **(Normalized)**

Fig. 6.19 Comparison on the soil blocking effect (ECM-C-30-SB & ECM-C-30, C_d=1.6)

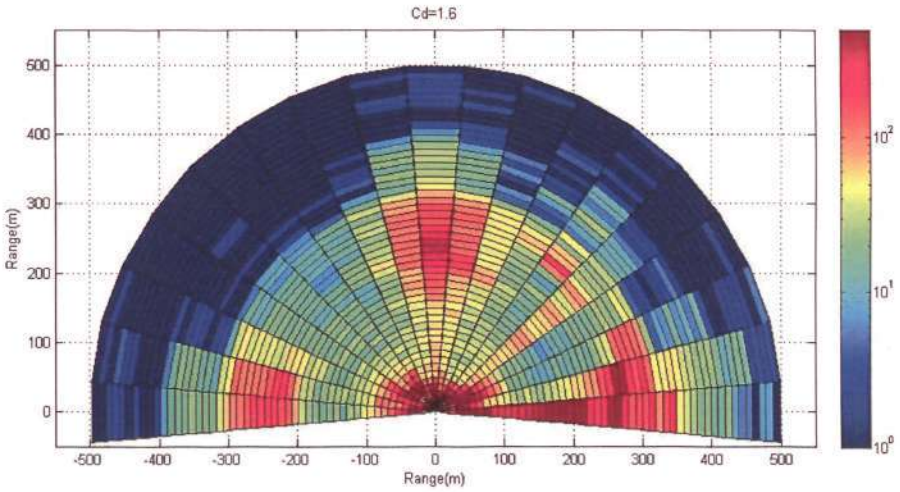

(a) Scattering map of case ECM-D-30-SB

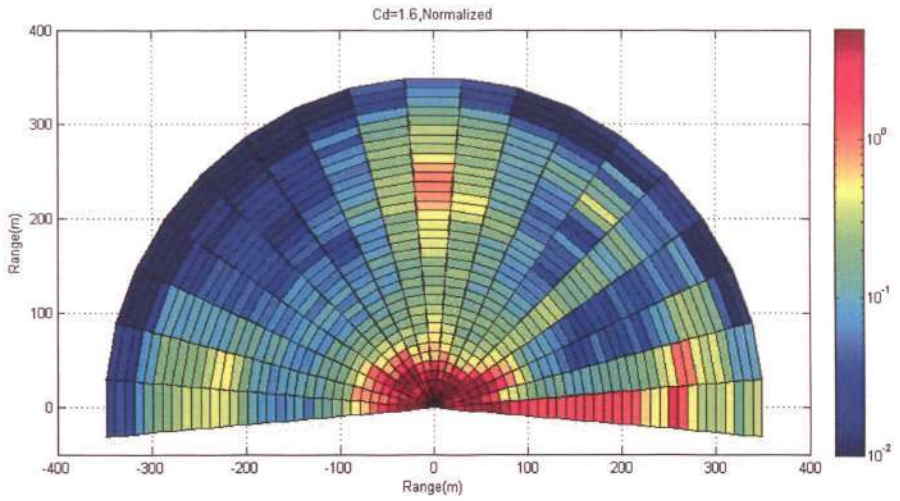

(b) Scattering map of case ECM-D-30-SB (Normalized)

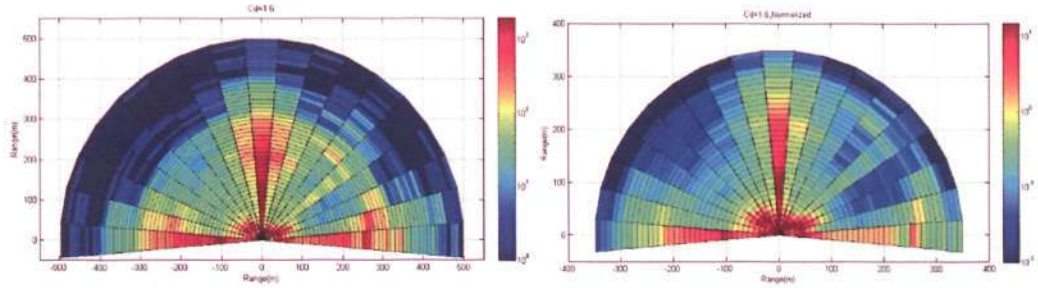

(c) Scattering map of case ECM-D-30 **(Normalized)**

Fig. 6.20Comparison on the soil blocking effect (ECM-D-30-SB & ECM-D-30, C_d=1.6)

Observed from Fig. 6.11 to Fig. 6.18, the debris scattering patterns are in good agreement with the foregoing analyses in Sections 6.4.2~ 6.4.5. High debris number counts are found in the direction normal to the three walls. Also, high-density loads result in higher ejecting velocities which in turn, lead to larger debris flying range and higher debris number count.

The soil cover reduces the debris ejecting velocities and thus results in a more compact scattering pattern, as can be seen in all diagrams comparing the distribution patterns between earth-covered and uncovered magazine.

The blocking effect of the soil adjacent to the three walls is significant. As can be easily detected from Fig.6.19 and Fig. 6.20, the reduction in debris number count outside the back wall and the 2 side walls is obvious. The zone outside the front wall is not affected.

6.5 Summary

Attention is focused on the high-density load cases, since the low-density load only leads to badly structural damage but with few number of debris.

Tracing the free-flying motion of debris needs a scientific deduction for a reasonable range of drag coefficients C_d, likely between 1.2 and 2.0. Using this range, the longest resulting debris flying range could be 150% of the shortest. A profound research on narrowing the appropriate range of C_d values is needed in future.

Soil cover is an effective means to reduce the debris flying range and the velocity range as well

7. Conclusions and recommendations

7.1 Conclusions

In this thesis, numerical simulation of debris throw after breaking up of a concrete structure by blast load has been carried out. The simulation results can be used to the debris risk analysis. The combination of the programs and the algorithm to simulate the debris throw is the most novel part of the thesis.

In chapter 2, research on kinds of debris was reviewed. Debris from various sources were covered. Several debris risk analysis models and prediction tools were introduced followed by the tests against the predictions.

Debris motion and drag force were discussed in chapter 3 and chapter 4. The debris motion was 2D and spinning motion was excluded. The debris was subjected to gravity force and drag force and the specific attention was made to the drag coefficient in drag force equation. The drag coefficients, which were C_d = 1.2, 1.6 and 2.0, used in the calculation are determined based on the published tests results and scientific judgment.

The algorithms employed in LS-DYNA and in the C++ program were introduced in chapter 5. As the simulation was the corporation done by LS-DYNA and in C++ program, data delivering and re-managing ware presented. As a result of re-managing, the debris was defined in C++ program. The validity of the debris simulation was approved as well.

Chapter 6 presented the information of the model and simulation results. Simulations were done to investigate the deformation, fracture and breakup of earth covered/uncovered magazine under internal detonation with consideration of different charge stack formats (centered and distributed) and different loading

densities (2.5kg/m^3 and 30kg/m^3). Therefore, numerical simulations were carried out for various cases. Simulations for debris free-flying were performed after the blast overpressure dropped to zero. The debris scattering patterns were investigated and presented in statistical terms.

The results of break-up and deformation patterns were looked into. The conclusions are as followed.

Under high-density load of 30 kg/m^3, in all cases the concrete magazine was broken into debris. The soil cover had little effect on the structural integrity. In contrast, in all low-density loading cases, the magazine structure almost kept intact at the computational cut-off time, except for the AGM-C-2.5 case, which yielded very serious cracks and tended to break up.

In the simulation of debris throw, conclusions could be drawn as followed.

1) In general, the ECM cases yielded lower debris ejection velocities than the AGM cases did. Also, the distributed-charge cases led to lower debris ejection velocity than the centered-charge cases did. On the other hand, the soil cover had more significant effect on reducing the ejection velocity of debris generated from the roof in low-density load cases.

2) The soil cover was the most significant factor in reducing the debris flying range. The earth-covered magazine yielded a reduced hazard zone, measured in terms of velocity range or debris flying range.

3) The charge distribution format was another significant factor affecting the debris flying range, though it was as prominent as the soil cover.

4) The drag coefficient C_d was the key factor influencing the debris flying range. Results were derived for selected values of Cd ranging from1.2 to 2.0. Nevertheless, more in-depth investigation work needs to be done to find/verify the appropriate values of C_d for the debris throw motion.

7.2 Recommendations

Future research is recommended to include the factors below.

A cluster is a group of particles held together as result of hydrodynamic effects. The debris of very small size are likely to form this kind of cluster. Therefore, the cluster effects on the drag coefficient should be added into the research scope.

The debris motion in this thesis is 2D. However, the spinning motion affects the debris flying range. Attention should be made to find more about the more complex motion pattern, such like 3D or 6D.

In order to have a more complete understanding to the debris hazards, the investigation of phenomenon when and after debris hits the ground is necessary. The debris ricochet, bounce and break-up should be included in the debris risk analysis.

8. References

Abbott, I. H. and Von Doenhoff, A. E. (1959). Theory of Wing Sections: Including a Summary of Airfoil Data, Courier Dover Publications.

Baker, C. J. (2004). Solutions of the debris equations 6th U.K. Conference on Wind Engingeering Cranfield.

Barr, C. and Barnaud, G. (1995). "High Reynolds number simulation techniques and their application to shaped structures model test." Journal of Wind Engineering and Industrial Aerodynamics **57**(2-3): 145-157.

Berglund, R., Carlberg, A., et al. (2006). Break up tests with small "ammunition houses", FOI - Swedish Defense Research Agency.

Chudinov, P. S. (2001). "The motion of a point mass in a medium with a square law of drag." Journal of Applied Mathematics and Mechanics **65**(3): 421-6.

Chudinov, P. S. (2004). "Analytical investigation of point mass motion in midair." European Journal of Physics **25**(1): 73-9.

Clancy, L. J. (1975). Aerodynamics. London Pitman.

Dörr, A., van der Voort, M., et al. (2008). The Development and Application of the Klotz Group Software.

DDESB (1991). Prediction of Building Debris for Quantity-Distance Siting T.P.13 . .

FAA (a). Waivers: Aviation Events, Advisory Circular, Federal Aviation Administration**:** 32.

FAA (b). General Aviation Operations, Federal Aviation Administration.

Fan, L., Shen, W., et al. (2002). "The causes of flying rock and safety precautions in demolition blasting." Engineering Blasting **8**(1).

Fan, S. C., Yang, Y. W., et al. (2007). Methodology for numerical simulation of breaking up of RC box structure under high-density blast load.

Farell, C. (1981). "Flow around fixed circular cylinders: fluctuating loads." Journal of the Engineering Mechanics Division **107**(3): 565-588.

Fox, R. W. and McDonald, A. T. (1994). Introduction to Fluid Mechanics.

Gao, W. L. and Hu, F. (1996). "The outer ballistic study of blasting fly rock." Blasting **13**(1).

Gerhart, P. M., Gross, R. J., et al. (1992). Fundamentals of Fluid Mechanics, 2nd ed.

Hayen, J. C. (2003a). "Projectile motion in a resistant medium - Part I: Exact solution and properties." International Journal of Non-Linear Mechanics **38**(3): 357-369.

Hayen, J. C. (2003b). "Projectile motion in a resistant medium - Part II: Approximate solution and estimates." International Journal of Non-Linear Mechanics **38**(3): 371-380.

Hoerner, S. F. (1965). Fluid-Dynamic Drag: Practical information on aerodynamic drag and hydrodynamic resistance. New York, Published by the Author.

Holmes, J. D. and English, E. C. (2004). Aerodynamics and trajectories of windborne debris--Part 1: compact objects, Part 2: sheet objects. 11th Australasian Wind Engineering Society Workshop, Darwin, Astralia.

Holmes, J. D., Letchford, C. W., et al. (2006). "Investigations of plate-type windborne debris--Part II: Computed trajectories." Journal of Wind Engineering and Industrial Aerodynamics **94**(1): 21-39.

Kang, N. (1999). "Prevention Measures for Controlling Flyrock in Engineering Blasting." Blasting **16**(1).

Lee, A. J. H. (1974). "A general study of tornado-generated missiles." Nuclear Engineering and Design **30**: 418-433.

Lee, B. E. and Wills, J. (2002). "Vulnerability of fully glazed high-rise building in tropical cyclones." Journal of Architectural Engineering **8**(2).

Lewis, B. A. (2004). Manual for LS-DYNA Soil Material Model 147. FHWA-HRT-04-095, Federal Highway Administration, USA.

Lin, B. (1999). "An assumption of recovery two stage launch vehicle." Spacecraft recovery and remote sensing **20**(1): 5-11.

Lin, N. (2005). Simulation of Windborne Debris Trajectories, Texas Tech University. **master:** 1-2.

Lindemuth, J. (1971). "The effect of air resistance on falling balls." American Journal of Physics **39**(7): 757-9.

LS-DYNA (2003). Keyword User's Manual, Version 970, Livermore Software Technology Corporation.

LS-DYNA (2007). Keyword User's Manual, Version 971, Livermore Software Technology Corporation.

Lu, Y., Gong, S. F., et al. (2005). Numerical study of blast load simulation and development of comprehensive modeling scheme for improved concrete break-up simulation.

Lu Y., Tu Z.G., et al. (2006). Coupled Numerical Simulation of Concrete Box Structures with RC/Mixture RC Material Models and Case Studies. Singapore.

MacDonald, W. M. and Hanzely, S. (1991). "The physics of the drive in golf." American Journal of Physics **59**(3): 213-18.

McCallum, S. C., Locking, P. M., et al. (2008). Simulation of masonry wall failure and debris scatter. 6th European LS-DYNA User's Conference.

McDonald, J., R., (1976). Tornado-generated Missiles and Their Effects. Symposium on Tornadoes, Texas Tech University.

McDonald, J. R. (1990). "Impact resistance of common building materials to tornado missiles." Journal of Wind Engineering and Industrial Aerodynamics **36**: 717-742.

McDonald, J. R. (1999). Windborne debris impacts on metal wall panels and their implications. Wind Engineering into the 21st Century.

Minor, J. E. (1994). "Windborne debris and the building envelope." Journal of Wind Engineering and Industrial Aerodynamics **53**: 207-227.

Morales, D. A. (2005). "Exact expressions for the range and the optimal angle of a projectile with linear drag." Canadian Journal of Physics **83**(1): 67-83.

Munson, B. R., Young, D. F., et al. (2002). Fundamentals of fluid mechanics, John wiley & Sons, Inc.

Murman, S. M. (2005). Characterization of Space Shuttle Ascent Debris Aerodynamics Using CFD Methods. 43rd AIAA Aerospace Sciences Meeting. Reno, NV.

Nakamura, Y. and Tomonari, Y. (1982). "The effects of surface roughness on the flow past circular cylinders at high Reynolds numbers." Journal of Fluid Mechanics **123**: 363-78.

Nussbaumer, P. and Kummer, B. (2008). Debris throw hazard from vehicles transporting explosives. 33rd DoD Explosives Safety Seminar. California, U.S.

Oldham, H. E. j. (1990). Aircraft Debris Trajectory Analysis-A report on the ballistic trajectory characteristic and relative scatter patterns of in-flignt airframe separation debris, specific to the airshow environment. Andson, South Carolina.

Price, R. H. and Romano, J. D. (1998). "Aim high and go far-optimal projectile launch angles greater than 45&deg." American Journal of Physics **66**(2): 109-13.

Pu, A. X. (1985). Exterior ballistics. Beijing, National Defense Industry Press.

Pu, F. (1983). Exterior ballistics Beijing, National Defense Industry Press.

Qin, M. W. (1991). Controlled Blast Beijing, Metallurgical Industry Press.

Redmann, G. H., Radbill, J. R., et al. (1976). Wind field and trajectory models for tornado propelled objects. Technical Report No.1. Palo Alto, CA, Electrical Power Research Institute.

Reid, J. D., Coon, B. A., et al. (2004). Evaluation of LS-DYNA Soil Material Model 147. FHWA-HRT-04-094, Federal Highway Administration, USA.

Simiu, E. and Cordes, M. (1976). National Bureau of Standards.

Swisdak, M. M. J., Conway, R., et al. (2008). Project eskimore -The DDESB long-term testing initiative. 33rd DoD Explosives Safety Seminar California, U.S.

Tachikawa, M. (1983). "Trajectories of flat plates in uniform flow with application to wind-generated missiles." Journal of Wind Engineering and Industrial Aerodynamics **14**(1-3): 443-453.

Tan, A., Frick, C. H., et al. (1987). "The fly ball trajectory: an older approach revisited." American Journal of Physics **55**(1): 37-40.

Timmerman, P. and van der Weele, J. P. (1999). "On the rise and fall of a ball with linear or quadratic drag." American Journal of Physics **67**(6): 538-46.

Twisdale, L. A. (1979). "Tornado missile transport analysis." Nuclear Engineering and Design **51**: 295-308.

Twisdale, L. A., Vickery, P. J., et al. (1996). Analysis of hurricane windborne debris impact risk for residential structure, prepared for State Farm Mutual Automobile Insurance Companies.

van der Voort, M. (2008). The application of debris and fragment throw models in risk assessment methodologies. 33rd DoD Explosives Safety Seminar. California, U.S.

van der Voort, M. M., van Doormaal, J. C. A. M., et al. (2008). "A universal throw model and its applications." International Journal of Impact Engineering **35**: 109-118.

Vial, A. (2007). "Horizontal distance travelled by a mobile experiencing a quadratic drag force: normalized distance and parameterization." European Journal of Physics **28**(4): 657-63.

Warburton, R. D. H. and Wang, J. (2004). "Analysis of asymptotic projectile motion with air resistance using the Lambert W function." American Journal of Physics **72**(11): 1404-7.

Weerheijm, J., Norman, P., et al. (2008). Comparison of Debris Throw Modeling with KG-ET Software, SAFER and UK Approach Comparison of Debris Throw Modeling with KG-ET Software, SAFER and UK Approach

Yu Q.J., Yang Y.W., et al. (2008). A novel numerical approach for modeling break-up of reinforced concrete structure. 33rd DoD Explosives Safety Seminar California, U.S. **10**.

Zufiria, J. A. and Sanmartin, J. R. (1982). "Influence of air drag on the optimal hand launching of a small, round projectile." American Journal of Physics **50**(1): 59-64.

Черниговский, A. A. and Shi, J. Y., (Translation) (1982). Применение направленного взрыва в горном деле и строительстве(Directional Demolition Blasting). Beijing, China Architecture & Building Press.